

Entangling Power: A Probe of Symmetry and Integrability in Quantum Many-Body Systems

Ian Low*, Pallab Goswami

Department of Physics and Astronomy, Northwestern University, Evanston, IL 60208, USA

The entangling power of a unitary operator quantifies its ability to generate entanglement from product states and provides a natural probe of quantum many-body dynamics. Entanglement extremization at points of enhanced symmetry has previously been observed in high-energy scattering. In this work we compute the time-averaged entangling power of anisotropic Heisenberg spin chains across two-site models and finite-size systems, as well as the entangling power of the two-magnon S -matrix in the thermodynamic limit. For two-site models we establish a monotonic hierarchy: the entangling power decreases as the symmetry group grows, reaching its minimum at the $SU(2)$ XXX point. Finite-size XXZ chains exhibit sharp dips at the $SU(2)$ points $\Delta = \pm 1$ and the free-fermion point $\Delta = 0$, with the free-fermion dip decaying much more slowly with system size. In the thermodynamic limit, we decompose the two-magnon S -matrix into quantum logic gates—Identity, SWAP, and $\sigma_z \otimes \sigma_z$ —and show that the entangling power vanishes for all scattering energies at the $SU(2)$ points, where the S -matrix reduces to the Identity gate, while the free-fermion point achieves the maximum—the opposite of the finite-size many-body behavior. The entangling power can serve as an *operator* diagnostic for symmetry and selected aspects of integrability in quantum simulations of spin-chain dynamics.

I. INTRODUCTION

Symmetry is arguably the most powerful organizing principle in physics. From conservation laws and selection rules to the classification of fundamental interactions and phases of matter, symmetry considerations pervade nearly every branch of physics. Yet the origin of symmetry remains one of the deepest open questions and its existence always postulated rather than derived. Understanding *why* certain symmetries appear in nature, rather than merely categorizing them, is a challenge that may require fundamentally new organizing principles.

Recent developments at the intersection of quantum information science and fundamental physics provide a tantalizing hint that such a principle may exist. In low-energy nucleon-nucleon scattering, the entangling power of the S -matrix is minimized at the Wigner $SU(4)$ point, where spin and isospin symmetries combine into a larger group, as well as the unitarity limit when non-relativistic conformal invariance appears [1, 2]. Similar correlations between entanglement extremization and enhanced symmetry have been identified in a growing number of scattering processes under different contexts, including low-energy hadron dynamics [3–5], beyond-the-Standard-Model extensions for the Higgs boson [6–9], and the general S -matrix framework [10, 11]. These findings suggest that symmetry may emerge from an extremization principle rooted in quantum entanglement, offering a new perspective on its origin. In addition, further investigations suggest that extremization of quantum resources may predict fundamental constants in nature, such as the Cabibbo-Kobayashi-Maskawa matrix [12], weak mix-

ing angle [13], and the Higgs mass [14].

In quantum many-body physics, the interplay of entanglement and symmetry has been explored extensively, but through a rather different lens. Ground-state entanglement entropy [15, 16] and its area-law scaling [17, 18] have become central tools for characterizing quantum phases and critical points [19, 20]; see Refs. [21, 22] for reviews. Symmetry-resolved entanglement, which decomposes the entanglement entropy into contributions from sectors labeled by conserved charges, has attracted considerable attention as a refined probe [23–26]. These are powerful frameworks, but they share two limitations: they characterize a particular *state* (typically the ground state) rather than the dynamics itself, and symmetry-resolved entanglement requires knowing *a priori* the existence of conserved charges and, therefore, the symmetry.

In this work we take a fundamentally different approach. The entangling power, introduced in Refs. [27, 28], is a property of the *operator* U rather than any single state—it measures the average entanglement generated by U acting on product states drawn uniformly from the Haar measure. Crucially, no assumption about the symmetry of the system is needed; instead, the symmetry reveals itself through the behavior of the entangling power. When applied to the time-evolution operator $U(t) = e^{iHt}$ of a many-body Hamiltonian, the time-averaged entangling power $\overline{\text{ep}}$ captures the typical entanglement production of the dynamics [29, 30] and provides a symmetry probe complementary to existing state-level diagnostics. We compute $\overline{\text{ep}}$ for anisotropic Heisenberg spin chains across three regimes that are usually studied separately—two-site quantum gates, finite-size many-body chains, and the two-magnon S -matrix in the thermodynamic limit—and show that in every regime the entangling power is suppressed at points of enhanced algebraic structure. The entangling power thus functions as

*Corresponding author: ilow@northwestern.edu

a dynamical symmetry witness across scales, with practical implications for quantum simulation and Hamiltonian characterization: it diagnoses the symmetry content of the dynamics without reference to any particular eigenstate or ground state.

This paper is organized as follows. In Sec. II we review the entangling power and its time-averaged version. In Sec. III we present the two-site results, including the symmetry hierarchy, eigenvalue analysis, and isospectral decomposition. In Sec. IV we extend to finite-size spin-1/2 and spin-1 chains and study the persistence and decay of the symmetry dip, the emergence and mechanism of the free-fermion dip, and their contrasting scaling with system size. In Sec. V we disentangle the roles of symmetry and integrability by studying the J_1 - J_2 model and the bilinear-biquadratic spin-1 chain. In Sec. VI we introduce the six-vertex R -matrix that encodes two-magnon scattering in the XXZ chain, compute its entangling power as a function of rapidity and anisotropy, decompose it into quantum logic gates, and show that the correlation between entanglement suppression and symmetry enhancement extends to the thermodynamic limit. We conclude with a discussion in Sec. VII. A pedagogical derivation of the Bethe ansatz and the two-magnon S -matrix is provided in Appendix D.

II. ENTANGLING POWER

Quantum entanglement is ordinarily a property of a state: a given state vector in a bipartite Hilbert space $\mathcal{H}_A \otimes \mathcal{H}_B$, its degree of entanglement is quantified by an entanglement measure applied to the state. The entanglement *generated* by a unitary operator U , however, depends on the input state it acts on. A familiar example is the CNOT gate: acting on the computational-basis state $|0\rangle \otimes |0\rangle$ it produces the product state $|0\rangle \otimes |0\rangle$, while acting on $|+\rangle \otimes |0\rangle$ (with $|+\rangle = (|0\rangle + |1\rangle)/\sqrt{2}$) it produces the maximally entangled Bell state $(|00\rangle + |11\rangle)/\sqrt{2}$. To characterize the entangling capability of a unitary operator, one averages over input states.

The entangling power, introduced in Refs. [27, 28], does exactly this. Given a bipartite unitary U acting on $\mathcal{H}_A \otimes \mathcal{H}_B$ with $d_i = \dim \mathcal{H}_i$, one draws random states $|\psi\rangle \in \mathcal{H}_A$ and $|\phi\rangle \in \mathcal{H}_B$ independently from the Haar measure, applies U to the product state $|\psi\rangle \otimes |\phi\rangle$, and measures the entanglement of the output via the reduced density matrix $\rho_A = \text{Tr}_B(U|\psi, \phi\rangle\langle\psi, \phi|U^\dagger)$. One must choose an entanglement measure; following Refs. [27, 28] we adopt the linear entropy [31] $\mathcal{E}(|\psi\rangle) = 1 - \text{Tr}(\rho_A^2)$, which vanishes when $|\psi\rangle$ is a product state and is maximal for maximally mixed ρ_A [5]. The entangling power is then defined by averaging the linear entropy of the

output states over all product-state inputs [27, 28]:¹

$$\text{ep}(U) \equiv \frac{d_A}{d_A - 1} \overline{\mathcal{E}}, \quad (1)$$

where the overline denotes an average over Haar-random product states $|\psi\rangle \otimes |\phi\rangle$. The prefactor $d_A/(d_A - 1)$ normalizes the linear entropy so that $\text{ep}(U) = 0$ when U maps every product state to a product state (e.g., the identity or the SWAP gate) and $\text{ep}(U) = 1$ when the average entanglement is maximal. It is worth noting that this prefactor involves only d_A , the dimension of the subsystem whose reduced state is computed, while the dependence on d_B enters implicitly through the Haar average over $|\phi\rangle$. By construction, $\text{ep}(U)$ is a property of the unitary operator itself, not of any particular input state; it is also closely related to information scrambling and operator entanglement [32].

The Haar integrals in Eq. (1) can be evaluated analytically by mapping the problem to the doubled Hilbert space. The key idea is the operator–state correspondence: any operator O acting on a Hilbert space \mathcal{H} of dimension d can be mapped to a state $|O\rangle\rangle \in \mathcal{H} \otimes \mathcal{H}$ via $|O\rangle\rangle = (O \otimes \mathbf{1}) \sum_{i=1}^d |i\rangle|i\rangle$, where $\{|i\rangle\}$ is an orthonormal basis of \mathcal{H} . The Hilbert–Schmidt inner product of two operators then becomes the overlap of their corresponding states: $\langle\langle A|B\rangle\rangle = \text{Tr}(A^\dagger B)$. Applying this correspondence to $U^{\otimes 2}$ acting on $(\mathcal{H}_A \otimes \mathcal{H}_B)^{\otimes 2}$, the Haar averages reduce to traces of swap operators in the doubled space [27, 28]. Following the formulation of Ref. [33], the result can be expressed compactly as

$$\text{ep}(U) = 1 - C_{d_A} C_{d_B} \sum_{\alpha=0}^1 I_\alpha(U), \quad (2)$$

where $C_d = 1/[d(d+1)]$ and, for $\alpha = 0, 1$,

$$I_\alpha(U) = \text{Tr}(T_{1+\alpha, 3+\alpha} + \langle U^{\otimes 2}, T_{1+\alpha, 3+\alpha} \cdot U^{\otimes 2} \cdot T_{13} \rangle_{\text{HS}}). \quad (3)$$

Here T_{ij} denotes the transposition (swap) operator acting on the i th and j th tensor factors in $(\mathcal{H}_A \otimes \mathcal{H}_B)^{\otimes 2}$, and $\langle A, B \rangle_{\text{HS}} = \text{Tr}(A^\dagger B)$ is the Hilbert–Schmidt inner product. The advantage of this operator formulation is that it reduces the computation of $\text{ep}(U)$ to traces in the doubled Hilbert space, avoiding any explicit integration over random states.

A. An Algorithm for the Time-average

The time-evolution operator $U(t) = e^{iHt}$ of a time-independent Hamiltonian $H = \sum_n E_n |n\rangle\langle n|$ generates

¹ An alternative convention, used in Refs. [1, 5], omits the prefactor $d_A/(d_A - 1)$ in Eq. (1), defining the entangling power as the average of the unnormalized linear entropy.

a one-parameter family of unitaries, and we define the time-averaged entanglement power

$$\overline{\text{ep}} \equiv \lim_{T \rightarrow \infty} \frac{1}{T} \int_0^T \text{ep}(e^{iHt}) dt, \quad (4)$$

which depends only on the spectrum and eigenstates of the Hamiltonian H .

Although Eq. (4) can be calculated by brute-force, we present in the following an efficient algorithm for its computation. Since $\text{ep}(U(t))$ is quartic in the matrix elements of $U(t)$, the integrand involves oscillatory phases $e^{-i\omega t}$ where $\omega = E_m - E_n + E_p - E_q$. Since

$$\lim_{T \rightarrow \infty} \frac{1}{T} \int_0^T e^{-i\omega t} dt = \delta_{\omega,0}, \quad (5)$$

the infinite-time average retains only those combinations satisfying $\omega = 0$ —the diagonal-ensemble contribution. This enables an *exact* evaluation of $\overline{\text{ep}}$ for any system whose Hamiltonian can be diagonalized, without resorting to a finite integration window. We outline the steps of this algorithm, leaving the full details in Appendix A:

1. Diagonalize H to obtain eigenvalues $\{E_n\}$ and eigenvectors $\{|n\rangle\}$.
2. For each eigenvector $|n\rangle$, expand it in the product basis $\{|a\rangle \otimes |b\rangle\}$, where $\{|a\rangle\}$ and $\{|b\rangle\}$ are orthonormal bases for \mathcal{H}_A and \mathcal{H}_B respectively, and arrange the coefficients into a $d_A \times d_B$ matrix C_n with entries $(C_n)_{ab} = \langle a \otimes b | n \rangle$.
3. The diagonal-ensemble condition $E_m - E_n + E_p - E_q = 0$ is equivalent to $E_m - E_p = E_n - E_q$, i.e. two pairs of eigenstates contribute only when they share a common eigenvalue difference $\omega \equiv E_m - E_p = E_n - E_q$. Collect all pairs (k, l) with the same value of $\omega = E_k - E_l$ into a group g_ω ; only pairs within the same group contribute to $\overline{\text{ep}}$.
4. For each group g_ω containing N_g pairs, form the $d_A \times d_A$ matrix $M_i \equiv C_k C_l^\dagger$ for the i th pair, where k and l are the eigenvector indices of that pair. The contribution of this group to the time-averaged purity is $\sum_{i,j=1}^{N_g} |\text{Tr}(M_i^\dagger M_j)|^2$.
5. Sum over all groups to obtain the dynamical part of $\overline{I_0}$. For $\overline{I_1}$, form also the $d_B \times d_B$ matrices $\hat{M}_i \equiv C_k^\dagger C_l$ for each pair; the contribution of each group is then $\sum_{i,j=1}^{N_g} \text{Tr}(M_i^\dagger M_j) \cdot \text{Tr}(\hat{M}_i^\dagger \hat{M}_j)$. Adding the constant terms $\text{Tr}(T_{13})$ and $\text{Tr}(T_{24})$ from Eq. (3), the time-averaged entangling power $\overline{\text{ep}}$ follows via Eq. (2).

The procedure requires only a single diagonalization and linear algebra on $d_A \times d_B$ matrices, and is practical for any system size where exact diagonalization is feasible. All time-averaged results in this work are computed by this method.

It is worth pointing out that the time-averaged entanglement power is determined by two ingredients: the eigenvalue spectrum and the eigenvector structure. The spectrum controls the grouping: eigenvalue degeneracies enlarge the groups g_ω , increasing the number of pairs that contribute to the sums in steps 4 and 5. The eigenvectors, through the coefficient matrices C_n , determine the magnitude of each trace factor $\text{Tr}(M_i^\dagger M_j)$ and $\text{Tr}(\hat{M}_i^\dagger \hat{M}_j)$. More symmetry typically produces more degeneracies, increasing the time-averaged purity $\overline{I_0 + I_1}$ and thereby suppressing $\overline{\text{ep}}$.

III. TWO-SITE SPIN CHAIN

We begin by investigating the entangling power in the simplest nontrivial setting: the two-site anisotropic Heisenberg Hamiltonian

$$H = a_x S_x \otimes S_x + a_y S_y \otimes S_y + a_z S_z \otimes S_z, \quad (6)$$

where S_i are the spin- s angular momentum operators acting on a d -dimensional Hilbert space at each site, with $d = 2s + 1$, and a_j 's are exchange constants. The time-evolution operator is $U(t) = e^{iHt}$. From the perspective of quantum information, the two-site spin chain is a bipartite quantum gate: spin-1/2 ($d = 2$) corresponds to a two-qubit unitary, spin-1 ($d = 3$) to a two-qutrit unitary, and general spin- s to a two-qudit system with local dimension d . This mapping places the entangling power of spin-chain Hamiltonians in direct contact with the theory of entangling gates in quantum computation and allows the results of this section to be read in either language.

The special cases of Eq. (6) include the isotropic XXX model ($a_x = a_y = a_z$), the XXZ model ($a_x = a_y, a_z = \Delta$), the XX model ($a_x = a_y, a_z = 0$), and the Ising model ($a_x = a_y = 0, a_z \neq 0$), among others. The two-site model is exactly solvable for arbitrary spin, and the analytical results presented below provide the intuition for the finite-size and thermodynamic-limit analyses in subsequent sections.

A. Spin-1/2 (Two-qubit)

For spin-1/2, the single-site operators are $S_i = \sigma_i/2$ with σ_i the Pauli matrices. The two-site Hilbert space has dimension $d_1 d_2 = 4$, the doubled space has dimension 16, and the normalization constant is $C_2 = 1/6$. A direct computation yields the closed-form entangling power

$$\begin{aligned} \text{ep}(U) = & \frac{1}{36} \left(6 - \cos[(a_x - a_y)t] - \cos[(a_x + a_y)t] \right. \\ & - \cos[(a_x - a_z)t] - \cos[(a_y - a_z)t] \\ & \left. - \cos[(a_x + a_z)t] - \cos[(a_y + a_z)t] \right), \quad (7) \end{aligned}$$

Model	(a_x, a_y, a_z)	Symmetry	N_0	$\overline{\text{ep}}$	Decimal
XYZ	all distinct	—	0	1/6	0.1667
XX	$(a, a, 0)$	$U(1)$	1	5/36	0.1389
XXZ (generic)	(a, a, Δ)	$U(1)$	1	5/36	0.1389
Ising	$(0, 0, a)$	$U(1)^2$	2	1/9	0.1111
XXX	(a, a, a)	$SU(2)$	3	1/12	0.0833

TABLE I: *Time-averaged entangling power for two-qubit models and their continuous symmetry groups.*

which involves six “frequencies” $a_x \pm a_y$, $a_x \pm a_z$, $a_y \pm a_z$. For the special cases of interest, Eq. (7) reduces to

$$\begin{aligned} \text{XXX: } \quad \text{ep} &= \frac{1}{6} \sin^2(at), \\ \text{Ising: } \quad \text{ep} &= \frac{2}{9} \sin^2(at/2), \\ \text{XX: } \quad \text{ep} &= \frac{1}{9} (3 + \cos(at)) \sin^2(at/2). \end{aligned} \quad (8)$$

The XXX result $\text{ep} = \frac{1}{6} \sin^2(at)$ has a transparent gate-theoretic interpretation. Using $\vec{\sigma}_1 \cdot \vec{\sigma}_2 = 2 \text{SWAP} - I$, the time-evolution operator can be written as

$$U(t) = e^{i\alpha(t)} [\cos(at/2) I - i \sin(at/2) \text{SWAP}], \quad (9)$$

where $\alpha(t)$ is an overall phase. At $at = 0$ one has $U = I$ (the identity gate), while at $at = \pi$ one has $U \propto \text{SWAP}$; these are the only two two-qubit gates with vanishing entanglement power [2]. The $\sin^2(at)$ oscillation thus traces the entanglement power of $U(t)$ as it interpolates between these two zero-entanglement gates.

Figure 1(a) shows $\text{ep}(U(t))$ as a function of time for the four models. The XXX model exhibits a clean single-frequency oscillation $\text{ep} \propto \sin^2(at)$, while the Ising model has a slightly richer pattern with period doubled. The XX model shows additional beating between its two distinct nonzero frequencies a and $2a$ (the remaining four of the six cosines in Eq. (7) collapse onto these two values when $a_x = a_y = a$, $a_z = 0$), and the XYZ model, with all six frequencies active, produces the most complex oscillatory structure. Despite this diversity in the time dependence, the time averages (dashed lines) respect the symmetry hierarchy in every case.

The infinite-time average of $\cos(\omega t)$ vanishes for $\omega \neq 0$ and equals 1 for $\omega = 0$. From Eq. (7), the time-averaged entangling power is therefore

$$\overline{\text{ep}} = \frac{6 - N_0}{36}, \quad (10)$$

where N_0 is the number of the six frequencies that vanish. Greater symmetry among the couplings forces more frequency differences to zero, directly reducing $\overline{\text{ep}}$. Table I lists $\overline{\text{ep}}$ for each model, and the resulting hierarchy is

$$\overline{\text{ep}}_{\text{XYZ}} > \overline{\text{ep}}_{\text{XX}} = \overline{\text{ep}}_{\text{XXZ}} > \overline{\text{ep}}_{\text{Ising}} = \overline{\text{ep}}_{\text{XX}} > \overline{\text{ep}}_{\text{XXX}}. \quad (11)$$

To understand the ordering of $\overline{\text{ep}}$ values in Table I, it is helpful to identify the continuous symmetries of

each model. A direct computation of the commutators $[S_i^{\text{tot}}, H]$ yields

$$[S_z^{\text{tot}}, H] = i(a_x - a_y)(S_{y,1} S_{x,2} + S_{x,1} S_{y,2}), \quad (12)$$

and cyclic permutations for S_x^{tot} and S_y^{tot} . Thus S_z^{tot} is conserved if and only if (iff) $a_x = a_y$, and similarly S_x^{tot} iff $a_y = a_z$, and S_y^{tot} iff $a_z = a_x$. The XYZ model, with all couplings distinct, has no continuous symmetry. The XXZ and XX models, with $a_x = a_y$, conserve S_z^{tot} and thus have $U(1)$ symmetry. The Ising model $H = a S_z \otimes S_z$ commutes with $S_{z,1}$ and $S_{z,2}$ independently—the spin projection at each site is separately conserved—giving $U(1) \times U(1)$, which has *more* continuous symmetry than XXZ or XX despite involving only one nonzero coupling. At the XXX point all three components of $\vec{S}^{\text{tot}} = \vec{S}_1 + \vec{S}_2$ are conserved, promoting the symmetry to $SU(2)$. The resulting symmetry hierarchy is none (XYZ) $\subset U(1)$ (XXZ/XX) $\subset U(1) \times U(1)$ (Ising) $\subset SU(2)$ (XXX), with dimensions 0, 1, 2, 3. As the dimension grows, the number of vanishing frequencies N_0 increases in lockstep: each new conserved charge enforces additional degeneracies in the eigenvalue spectrum, which in turn forces more oscillatory terms to average to zero, directly suppressing $\overline{\text{ep}}$.

B. Spin-1 (Two-qutrit)

For spin-1, the single-site operators are the standard 3×3 angular momentum matrices. The two-site Hilbert space has dimension $d_1 d_2 = 9$, the doubled space in Eq. (3) has dimension 81, and $C_3 = 1/12$. The transposition operators T_{13} and T_{24} are 81×81 permutation matrices with $\text{Tr}(T_{13}) = \text{Tr}(T_{24}) = 27$. The eigenvalue structure is considerably richer than the spin-1/2 case, as we will see.

Analytic computation yields closed-form expressions for the XXX, Ising, and XXZ models. For the general XYZ model the time averages are obtained by numerically diagonalizing H and then performing the exact infinite-time average using the eigenvalue-grouping algorithm described in Sec. II A.

a. *XXX* ($a_x = a_y = a_z = a$).

$$\begin{aligned} \text{ep} = \frac{1}{648} & \left(156 - 15 \cos(at) - 6 \cos(2at) \right. \\ & \left. - 65 \cos(3at) - 60 \cos(4at) - 10 \cos(6at) \right). \end{aligned} \quad (13)$$

This involves harmonics at frequencies $a, 2a, 3a, 4a, 6a$, considerably richer than the single-frequency spin-1/2 result $\text{ep} = (1/6) \sin^2(at)$.

b. *Ising / XX* ($a_x = a_y = 0$, $a_z = a$).

$$\text{ep} = \frac{1}{36} \left(9 - 4 \cos(at) - 4 \cos(2at) - \cos(4at) \right). \quad (14)$$

By relabeling of spin components, this formula applies to all single-coupling models (XX, YY, ZZ).

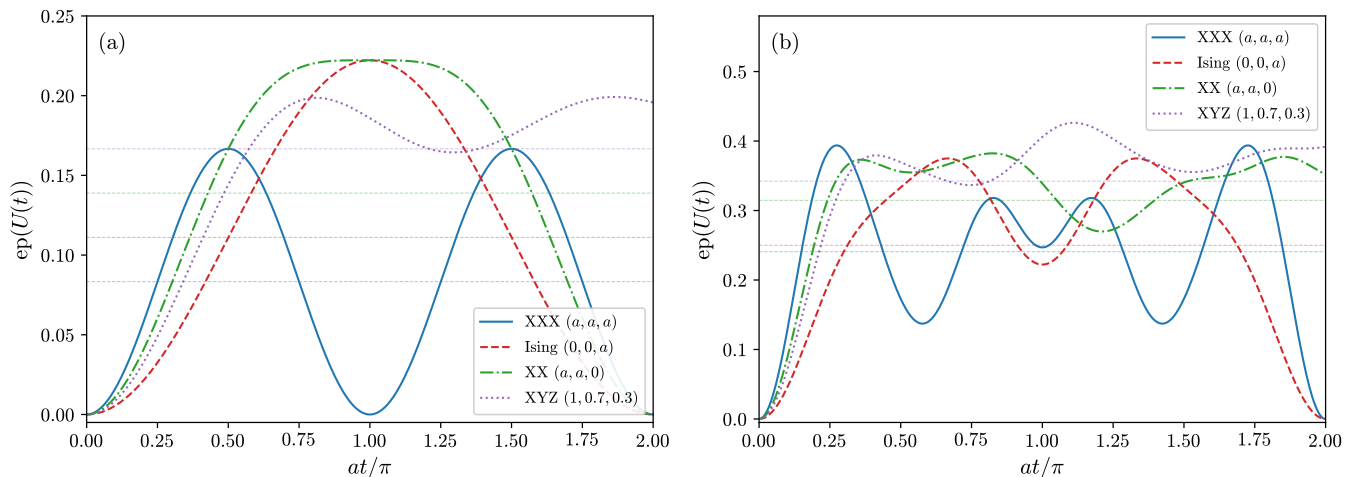


FIG. 1: Instantaneous $ep(U(t))$ of the two-site Hamiltonian (6) as a function of time at/π for the XXX (solid), Ising (dashed), XX (dash-dotted), and XYZ (dotted) models. (a) Spin-1/2 (two-qubit, $d = 2$). (b) Spin-1 (two-qutrit, $d = 3$). For the XYZ model we use $(a_x, a_y, a_z) = (1, 0.7, 0.3)$. Thin dashed horizontal lines indicate the time-averaged values \overline{ep} .

c. XX ($a_x = a_y = a, a_z = 0$).

$$\begin{aligned} ep = & \frac{1}{2304} \left(725 - 128 \cos(2at) - 48 \cos(4at) \right. \\ & - 192 \cos(\sqrt{2}at) - 92 \cos(2\sqrt{2}at) \\ & - 9 \cos(4\sqrt{2}at) - 96 \cos[(\sqrt{2}-2)at] \\ & - 32 \cos[2(\sqrt{2}-1)at] - 32 \cos[2(\sqrt{2}+1)at] \\ & \left. - 96 \cos[(\sqrt{2}+2)at] \right). \end{aligned} \quad (15)$$

The appearance of irrational frequencies ($\sqrt{2}a$, etc.) reflects the eigenvalue structure of the combined $S_x \otimes S_x + S_y \otimes S_y$ Hamiltonian.

d. XXZ ($a_x = a_y = 1, a_z = \Delta$). The instantaneous entangling power takes the form of a trigonometric polynomial with 24 frequencies:

$$ep(t) = \frac{5}{8} - \frac{1}{144} \left[\mathcal{A}_0 + \sum_{j=1}^{24} \mathcal{A}_j \cos(\Omega_j t) \right], \quad (16)$$

where the DC component is $\mathcal{A}_0 = (46\Delta^4 + 684\Delta^2 + 2636)/(\Delta^2 + 8)^2$. Of the 24 frequencies, 8 are rational:

$$\begin{aligned} \sum_{j \in R} \mathcal{A}_j \cos(\Omega_j t) = & \frac{4}{\Delta^2 + 8} \cos(\Delta t) \\ & + \frac{2\Delta^2}{\Delta^2 + 8} \left[\cos((\Delta+2)t) + \cos((\Delta-2)t) \right] \\ & + 4 \left[\cos((2\Delta+2)t) + \cos((2\Delta-2)t) \right] \\ & + \frac{8}{\Delta^2 + 8} \cos(3\Delta t) + 2 \cos(4\Delta t) \\ & + 3 \cos(4t), \end{aligned} \quad (17)$$

and the remaining 16 involve the irrational quantity $\zeta \equiv \sqrt{\Delta^2 + 8}$ through frequencies such as $\zeta, (3\Delta \pm \zeta)/2, (\Delta \pm$

$\zeta)/2 \pm 2$, etc. These are tabulated in full in Table III; the complete derivation of both the instantaneous and time-averaged formulas is given in Appendix C.

Time averaging kills all oscillating terms, leaving only the DC component. After simplification, the irrational eigenvalues $E_{\pm} = (-\Delta \pm \zeta)/2$ cancel pairwise, yielding the closed-form result

$$\overline{ep}(\Delta) = \frac{11\Delta^4 + 189\Delta^2 + 781}{36(\Delta^2 + 8)^2}, \quad (18)$$

valid for generic Δ .

Fig. 1(b) shows the instantaneous entangling power for the spin-1 models. The richer harmonic content compared to spin-1/2 is apparent: the XXX model now involves five frequencies ($a, 2a, 3a, 4a, 6a$) rather than a single one, and the XX model exhibits irrational-frequency beating that never recurs exactly. Nevertheless, the time averages (dashed lines) again respect the symmetry hierarchy.

The time-averaged values, obtained from the constant terms in the above expressions, are collected in Table II. The hierarchy is qualitatively the same as for spin-1/2:

$$\overline{ep}_{XYZ} > \overline{ep}_{XXZ} > \overline{ep}_{XX} > \overline{ep}_{\text{Ising}} = \overline{ep}_{XX} > \overline{ep}_{XXX}. \quad (19)$$

It is worth noting that, unlike spin-1/2, the XX and generic XXZ values now differ: the XX model gives $\overline{ep} = 725/2304 \approx 0.315$, while Eq. (18) evaluated at $\Delta = 0$ gives $781/2304 \approx 0.339$. The degeneracy $\overline{ep}_{XX} = \overline{ep}_{XXZ}$ seen in the $d = 2$ case is thus broken for spin-1; the origin of this splitting will become clear in the eigenvalue analysis of Sec. III C.

The analytic formula Eq. (18) and the degenerate-point values are displayed in Fig. 2. The generic curve is nearly flat, with a shallow minimum at $\Delta = 0$ (where $\overline{ep} = 781/2304 \approx 0.339$) and a plateau at $11/36 \approx 0.306$

Model	(a_x, a_y, a_z)	Symmetry	$\overline{\text{ep}}$ (exact)	Decimal
XYZ	(1, 0.5, 0.25)	—	—	0.371
XYZ	(1, 0.7, 0.3)	—	—	0.377
XXZ	(1, 1, 0.5)	$U(1)$	Eq. (18)	0.338
XX	$(a, a, 0)$	$U(1) \times \mathbb{Z}_2$	$725/2304$	0.315
Ising	$(0, 0, a)$	$U(1)^2$	$1/4$	0.250
XXX	(a, a, a)	$SU(2)$	$13/54$	0.241

TABLE II: Time-averaged entangling power for spin-1 models and their continuous symmetry groups.

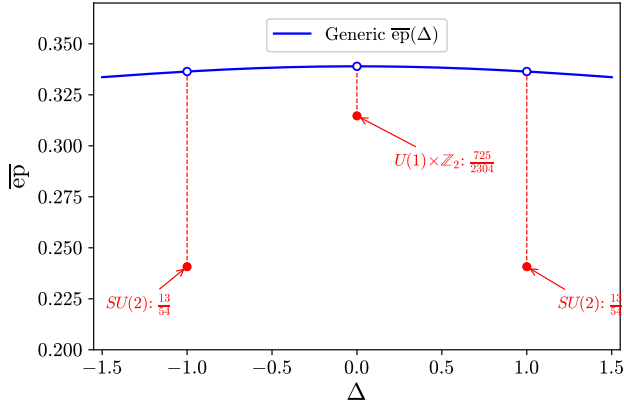


FIG. 2: Time-averaged entangling power of the two-site spin-1 XXZ model as a function of anisotropy Δ . The solid curve is the generic analytic formula, Eq. (18). At $\Delta = \pm 1$ ($SU(2)$ symmetry) and $\Delta = 0$ ($U(1) \times \mathbb{Z}_2$ symmetry), eigenvalue degeneracies result in the true $\overline{\text{ep}}$ (filled circles) dropping below the generic curve (open circles). Dashed lines indicate the magnitude of each dip.

for $|\Delta| \rightarrow \infty$. Superimposed on this smooth background are sharp dips at $\Delta = \pm 1$ (where $SU(2)$ symmetry introduces additional eigenvalue degeneracies, giving $\overline{\text{ep}} = 13/54$) and a milder dip at $\Delta = 0$ (where a \mathbb{Z}_2 spectrum-flipping symmetry forces further degeneracies, giving $\overline{\text{ep}} = 725/2304$). We now identify the symmetry at each of these special points.

e. $\Delta = \pm 1$: $SU(2)$ symmetry. At $\Delta = 1$ the XXZ Hamiltonian becomes the isotropic XXX model, with full $SU(2)$ symmetry. The dip at $\Delta = -1$ is exactly as deep, $\overline{\text{ep}}(-1) = \overline{\text{ep}}(1)$, as a consequence of local unitary equivalence. Define π -rotations about the x and y axes, $W_x = e^{i\pi S_x}$ and $W_y = e^{i\pi S_y}$, which act on the spin operators as

$$\begin{aligned} W_x &: (S_x, S_y, S_z) \rightarrow (S_x, -S_y, -S_z), \\ W_y &: (S_x, S_y, S_z) \rightarrow (-S_x, S_y, -S_z). \end{aligned} \quad (20)$$

Under the local unitary $W_x \otimes W_y$, the Hamiltonian transforms as

$$\begin{aligned} (W_x \otimes W_y) H(a_x, a_y, a_z) (W_x \otimes W_y)^\dagger \\ = H(-a_x, -a_y, a_z). \end{aligned} \quad (21)$$

Applied to the XXZ point $(1, 1, -\Delta)$, this gives $H(-1, -1, -\Delta) = -H(1, 1, \Delta)$. Since the entangling power satisfies $\text{ep}(e^{-iHt}) = \text{ep}(e^{iHt})$, the time averages are identical: $\overline{\text{ep}}(1, 1, -\Delta) = \overline{\text{ep}}(1, 1, \Delta)$. Note that this argument is valid for any spin d , not just spin-1.

f. $\Delta = 0$: \mathbb{Z}_2 spectrum-flipping symmetry. At $\Delta = 0$ the model reduces to $H = S_x \otimes S_x + S_y \otimes S_y$ (the XX model). This Hamiltonian possesses a discrete \mathbb{Z}_2 symmetry generated by $W = e^{i\pi S_{z,1}}$ acting on site 1 alone, which satisfies $W S_z W^\dagger = S_z$ but $W S_\pm W^\dagger = -S_\pm$. This implies $(W \otimes I) H (W \otimes I)^\dagger = -H$, so the spectrum is symmetric about zero: for every eigenvalue E , $-E$ is also an eigenvalue with the same degeneracy. This spectrum-flipping symmetry forces additional eigenvalue degeneracies that suppress $\overline{\text{ep}}$ below the generic XXZ value. It is worth noting that, for spin-1/2, $\Delta = 0$ is also the free-fermion point via the Jordan-Wigner transformation; this connection will play an important role in Sec. VI B.

C. Eigenvalue analysis

The mechanism behind the correlation between symmetry and entanglement suppression can be understood from the spectral decomposition of the time-evolution operator. Writing $U(t) = \sum_k e^{iE_k t} P_k$, where P_k is the projector onto the eigenspace of eigenvalue E_k , and recalling from Sec. II A that the infinite-time average retains only terms satisfying the diagonal-ensemble condition $E_m - E_n + E_p - E_q = 0$, the time-averaged entangling power depends in general on two ingredients: the eigenvalue spectrum (which controls which terms survive the time average) and the eigenvectors (which determine the matrix elements of those surviving terms). Recall that the time-averaging algorithm of Sec. II A partitions eigenstate pairs into ω -groups sharing the same energy difference. When a symmetry enforces eigenvalue degeneracies, pairs that would belong to separate groups at generic coupling are merged into larger groups, and the coherent sum within each enlarged group enhances the purity sums, thereby suppressing $\overline{\text{ep}}$. As we now discuss, the spin-1/2 case is special in that the eigenvectors are coupling-independent, so $\overline{\text{ep}}$ is determined entirely by the eigenvalue spectrum. For spin-1, both ingredients play a role.

a. Spin-1/2. The Hamiltonian (6) has eigenvalues

$$E \in \left\{ \frac{-a_x - a_y - a_z}{4}, \frac{a_x + a_y - a_z}{4}, \frac{a_x - a_y + a_z}{4}, \frac{-a_x + a_y + a_z}{4} \right\}, \quad (22)$$

and, crucially, the eigenvectors are the four Bell states independent of the coupling constants a_x, a_y, a_z . Because the projectors P_k are universal, the time-averaged entangling power depends *only* on the eigenvalue spectrum. Moreover, the closed-form expression Eq. (7)

shows that this dependence takes a particularly simple form: six cosine terms, each with equal weight $1/36$, giving $\overline{ep} = (6 - N_0)/36$ [Eq. (10)], where N_0 is the number of the six frequencies $a_x \pm a_y, a_x \pm a_z, a_y \pm a_z$ that vanish. The quantity N_0 therefore determines \overline{ep} completely, and models sharing the same N_0 necessarily share the same \overline{ep} —this is why the XXZ and XX models, despite having different eigenvalue structures, both give $\overline{ep} = 5/36$: each has exactly one vanishing frequency ($a_x - a_y = 0$), so $N_0 = 1$. The values of N_0 for all models are already listed in Table I.

At the XXX point, the four eigenvalues collapse to just two distinct values: $E = -3a/4$ (singlet, $S = 0$) and $E = a/4$ (triplet, $S = 1$). The $SU(2)$ symmetry forces the degeneracy $E_2 = E_3 = E_4$, which causes three of the six frequencies to vanish simultaneously ($N_0 = 3$), yielding the minimum $\overline{ep} = 1/12$.

This equal-weight simplicity—in which N_0 alone determines \overline{ep} —is specific to spin-1/2 and relies on the universality of the Bell-state eigenvectors. For spin-1, the eigenvectors depend on the coupling constants and a more refined analysis is needed.

b. Spin-1. The eigenvalues for the key models are: XXX $\{-2a, -a, a\}$ with degeneracies $\{1, 3, 5\}$ ($S = 0, 1, 2$); Ising $\{-a, 0, a\}$ with degeneracies $\{2, 5, 2\}$; and XX $\{-\sqrt{2}a, -a, 0, a, \sqrt{2}a\}$ with degeneracies $\{1, 2, 3, 2, 1\}$.

Unlike the spin-1/2 case, the eigenvectors of the spin-1 Hamiltonian *do* depend on the coupling constants. At the XXX point, $SU(2)$ symmetry organizes the 9 two-site states into irreducible representations of total spin: $S = 0$, $S = 1$, and $S = 2$, with eigenvalues $-2a$, $-a$, and a , respectively. Away from the isotropic point, the eigenstates are no longer organized by total spin.

Following the algorithm of Sec. II A, we partition the $d^4 = 81$ ordered pairs (k, l) of eigenstates into ω -groups labeled by $\omega = E_k - E_l$. The diagonal-ensemble condition $E_m - E_n = E_p - E_q$ is satisfied whenever (m, n) and (p, q) belong to the same ω -group. The number of distinct ω -groups for each model is: XYZ (61), XXZ (27), XX (13), XXX (7), and Ising (5). The XYZ and XXZ counts are generic values; specific parameter choices can produce accidental degeneracies that reduce the count. Note that the XX model has the same eigenvalue structure as Ising by rotational equivalence, and hence the same $\overline{ep} = 1/4$.

The ordering of \overline{ep} broadly tracks the ω -group count: more groups means more independent oscillatory terms survive the time average, leading to a smaller $\overline{I_0 + I_1}$ and hence a higher \overline{ep} . However, the ω -group count alone does not determine \overline{ep} for spin-1, since the eigenvectors—unlike the spin-1/2 case—depend on the coupling constants and enter the time-averaged purities through the matrix elements $\text{Tr}_A(M_i^\dagger M_j)$. The XXX model, with 7 groups, achieves $\overline{ep} = 13/54 \approx 0.241$, lower than the Ising model's $\overline{ep} = 1/4 = 0.250$ with only 5 groups. To disentangle the eigenvalue and eigenvector contributions to this suppression, we turn to the isospectral decomposition in the next subsection.

D. Isospectral decomposition

The eigenvalue analysis of the preceding subsection shows that eigenvalue degeneracy counting alone cannot fully explain the suppression of \overline{ep} at symmetric points, particularly for spin-1. To isolate the eigen-vector contribution, we construct isospectral families—Hamiltonians sharing the same spectrum as the XXX model but with different eigenstates—and compute their entangling power.

a. Uniqueness of the XXX degeneracy. We first ask whether the XXX model is the *only* member of the XYZ family in Eq. (6) with the XXX eigenvalue degeneracy pattern. For spin-1/2, the eigenvalue degeneracy pattern $\{1, 3\}$ requires all three triplet eigenvalues in Eq. (22) to coincide, which forces $a_x = a_y = a_z$ —precisely the XXX point. Moreover, sign-flipping local unitaries of the form $e^{i\pi S_\alpha} \otimes I$ map $(a_x, a_y, a_z) \mapsto (\pm a_x, \pm a_y, \pm a_z)$ (with exactly two sign flips), so any XYZ point with $|a_x| = |a_y| = |a_z|$ is locally unitarily equivalent to the XXX model. The $\{1, 3\}$ degeneracy pattern is therefore unique to the XXX local-unitary equivalence class.

For spin-1, the general XYZ Hamiltonian does not commute with S_z^{tot} , but it does commute with the $\mathbb{Z}_2 \times \mathbb{Z}_2$ parity operators $R_\alpha \equiv e^{i\pi S_{\alpha,1}} \otimes e^{i\pi S_{\alpha,2}}$ for $\alpha = x, y, z$. Since a π -rotation about the α -axis preserves S_α and flips the other two components, each bilinear term $S_{\beta,1} S_{\beta,2}$ picks up two sign flips that cancel, giving $[R_\alpha, H] = 0$. As shown in Appendix B, the 9×9 Hilbert space decomposes under (R_z, R_x) into four sectors of dimension $3 + 2 + 2 + 2$. The three two-dimensional sectors have eigenvalues $\pm a_z$, $\pm a_x$, and $\pm a_y$, respectively, while the three-dimensional sector has the following characteristic polynomial:

$$p(\lambda) = \lambda^3 - (a_x^2 + a_y^2 + a_z^2)\lambda + 2a_x a_y a_z. \quad (23)$$

For the XXX degeneracy pattern $\{1, 3, 5\}$, the 5-fold degenerate eigenvalue must appear in all four sectors, which forces $|a_x| = |a_y| = |a_z|$. Consistency with Eq. (23) is confirmed by the identity $p(a_x) = -a_x(a_y - a_z)^2$, so that a_x is a root of p if and only if $a_y = a_z$. Cyclic permutations then force $a_x = a_y = a_z$ —again the XXX point (up to local unitary equivalence via sign flips).

In fact, the $\mathbb{Z}_2 \times \mathbb{Z}_2$ decomposition derived in Appendix B makes it possible to compute \overline{ep} for the XXZ model in Eq. (18); the detail is given in Appendix C.

b. Isospectral family on $\mathbb{C}\mathbb{P}^3$. In the remainder of this subsection we restrict to spin-1/2 where the two-site Hilbert space \mathbb{C}^4 is simple and straightforward to analyze. Having established that the XXX degeneracy pattern is unique within the XYZ family, we now consider Hamiltonians *outside* this family that share the XXX spectrum $\{-3J/4, J/4, J/4, J/4\}$ but have different eigenstates. The eigenstate for $-3J/4$ can be parameterized by a normalized vector $|z\rangle \in \mathbb{C}\mathbb{P}^3$ with the corresponding projector $|z\rangle\langle z|$. The Hamiltonian is then

$$H = \frac{J}{4} \mathbf{1} - J |z\rangle\langle z| \quad (24)$$

which satisfies $H|z\rangle = (-3J/4)|z\rangle$. The rank-3 projector $\mathbf{1} - |z\rangle\langle z|$ then spans the eigenspace with eigenvalue $J/4$. The isospectral family is thus parametrized by $\mathbb{CP}^3 = U(4)/(U(3) \times U(1))$, a 6-dimensional manifold. The XXX model corresponds to $|z\rangle$ being the maximally entangled Bell state $(|01\rangle - |10\rangle)/\sqrt{2}$.

c. Spin-operator representation. To make explicit the physical content of the isospectral Hamiltonian in Eq. (24), we expand the projector $|z\rangle\langle z|$ in the operator basis $\{\mathbf{1}, \sigma_i\} \otimes \{\mathbf{1}, \sigma_j\}$. Writing $|z\rangle = (z_1, z_2, z_3, z_4)$ in the computational basis with $\sum_k |z_k|^2 = 1$, the completeness of the Pauli basis gives

$$|z\rangle\langle z| = \frac{1}{4}\mathbf{1} + \frac{1}{2}\sum_i \langle\sigma_i\rangle_1 S_{i,1} + \frac{1}{2}\sum_i \langle\sigma_i\rangle_2 S_{i,2} + \sum_{i,j} \langle\sigma_i \otimes \sigma_j\rangle S_{i,1} S_{j,2}, \quad (25)$$

where $\langle \dots \rangle$ denotes the expectation value in $|z\rangle$. The identity piece cancels the $\frac{J}{4}\mathbf{1}$ in Eq. (24), leaving

$$H = -\frac{J}{2}\sum_i \left(\langle\sigma_i\rangle_1 S_{i,1} + \langle\sigma_i\rangle_2 S_{i,2} \right) - J\sum_{i,j} \langle\sigma_i \otimes \sigma_j\rangle S_{i,1} S_{j,2}. \quad (26)$$

The most general isospectral Hamiltonian is therefore a bilinear spin-spin coupling with single-site Zeeman fields. All 15 parameters (9 couplings and 6 field components) are fixed by the 6 real parameters of $|z\rangle \in \mathbb{CP}^3$.

It is instructive to verify Eq. (26) in two limiting cases. For the XXX model, $|z\rangle = (|01\rangle - |10\rangle)/\sqrt{2}$ (the singlet), all single-site expectations vanish and $\langle\sigma_i \otimes \sigma_j\rangle = -\delta_{ij}$, so that Eq. (26) reduces to $H = J\vec{S}_1 \cdot \vec{S}_2$ as expected. At the opposite extreme, taking $|z\rangle = |00\rangle$ (an unentangled product state) gives $\langle\sigma_z\rangle_1 = \langle\sigma_z\rangle_2 = 1$ as the only nonvanishing single-site expectations and $\langle\sigma_z \otimes \sigma_z\rangle = 1$ as the only nonvanishing correlator. Equation (26) then yields the product-state partner

$$H_{\text{prod}} = -\frac{J}{2}(S_{z,1} + S_{z,2}) - J S_{z,1} S_{z,2}, \quad (27)$$

an Ising interaction plus a longitudinal magnetic field, whose eigenstates $\{|00\rangle, |01\rangle, |10\rangle, |11\rangle\}$ are all product states with eigenvalues $\{-3J/4, J/4, J/4, J/4\}$, identical to the XXX model. Despite having the same spectrum, H_{prod} in Eq. (27) gives $\overline{\text{ep}}_{\text{prod}} = 1/9 \approx 0.1111$, which is *larger* than the XXX value $\overline{\text{ep}}_{\text{XXX}} = 1/12 \approx 0.0833$ by a factor of $4/3$. The gap between the two is purely an eigenvector effect.

d. Local-unitary equivalence and the entangling power. The XXX point and any other point in the isospectral family are related by a unitary transformation, $H(|z\rangle) = V H_{\text{XXX}} V^\dagger$ with $V \in SU(4)$. Such a transformation preserves the spectrum but in general changes $\overline{\text{ep}}$: the entangling power is invariant only under the subgroup of single-qubit (local) unitaries $SU(2) \otimes$

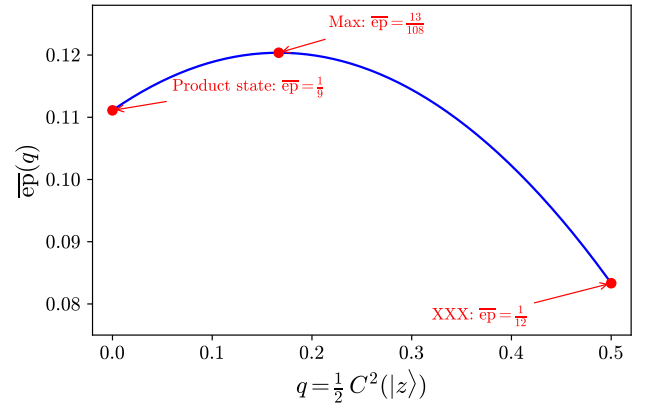


FIG. 3: Time-averaged entangling power of the spin-1/2 isospectral family, Eq. (29), as a function of $q = C^2(|z\rangle)/2$, where C is the concurrence of the projector state $|z\rangle$. The product-state limit ($q = 0$, $\overline{\text{ep}} = 1/9$) and the XXX/Bell-state limit ($q = 1/2$, $\overline{\text{ep}} = 1/12$) are marked, together with the maximum at $q = 1/6$. The XXX model sits at the minimum of $\overline{\text{ep}}$ over the isospectral family.

$SU(2) \subset SU(4)$. A generic $V \in SU(4)$ therefore generates a Hamiltonian with the same eigenvalues as H_{XXX} but a distinct entangling power.

e. Analytic formula for the isospectral family. The local-unitary structure above already determines on which property of $|z\rangle$ the entangling power can depend. Under a local unitary $|z\rangle \mapsto (u_A \otimes u_B)|z\rangle$, the Hamiltonian in Eq. (24) transforms as $H \mapsto (u_A \otimes u_B) H (u_A \otimes u_B)^\dagger$, and since $\overline{\text{ep}}$ is invariant under such conjugation, $\overline{\text{ep}}[H(|z\rangle)]$ is a local-unitary invariant of $|z\rangle$. For two-qubit pure states, every entanglement measure is a local-unitary invariant, and all such invariants are functionally equivalent to the concurrence $C(|z\rangle)$ [34, 35], as shown in Ref. [2]. Thus $\overline{\text{ep}}$ depends on $|z\rangle$ only through $C(|z\rangle)$, and we parametrize the family by

$$q = \frac{1}{2} C^2(|z\rangle). \quad (28)$$

The parameter q ranges from 0 (product state, $\alpha = 1$) to $1/2$ (Bell state, $\alpha = \beta = 1/\sqrt{2}$). Following the algorithm in Sec. II A, we obtain the time-averaged entangling power

$$\overline{\text{ep}}(q) = \frac{1 + q - 3q^2}{9}. \quad (29)$$

The product-state limit $q = 0$ gives $\overline{\text{ep}} = 1/9$, the Bell-state (XXX) limit $q = 1/2$ gives $\overline{\text{ep}} = 1/12$, and the maximum $\overline{\text{ep}} = 13/108$ occurs at $q = 1/6$.

The non-monotonic dependence on q is noteworthy: the entangling power initially *increases* as $|z\rangle$ acquires entanglement, reaches a maximum at $q = 1/6$, and then decreases as $|z\rangle$ approaches the Bell state. The XXX model, with maximally entangled eigenstates, sits at the *minimum* of $\overline{\text{ep}}$ over the isospectral family, confirming that the suppression of entanglement power at the $SU(2)$

point is driven by eigenvector structure, not just eigenvalue degeneracy. This non-monotonic behavior is displayed in Fig. 3.

IV. BEYOND TWO-SITE MODELS

The two-site results of the preceding section establish a clear correlation between symmetry enhancement and entanglement suppression. We now study this correlation beyond two-site models. In this Section we compute $\overline{\text{ep}}$ for spin chains of increasing length L and study the interplay between the growth of the Hilbert space and the richness of the many-body spectrum.

We consider spin-1/2 and spin-1 XXZ models [36] with open boundary conditions:

$$H_{\text{XXZ}} = \sum_{j=1}^{L-1} (S_x^{(j)} S_x^{(j+1)} + S_y^{(j)} S_y^{(j+1)} + \Delta S_z^{(j)} S_z^{(j+1)}), \quad (30)$$

where $S_i^{(j)}$ are the spin- s angular momentum operators at site j , with $s = 1/2$ or $s = 1$. We choose the equal bipartition $\{1, \dots, L/2\} | \{L/2 + 1, \dots, L\}$, so that $d_A = d_B = (2s + 1)^{L/2}$. The full Hilbert space has dimension $d = (2s + 1)^L$: for spin-1/2, the largest system we study is $L = 10$ ($d = 1024$), and for spin-1, $L = 6$ ($d = 729$). Time-averaged entangling power is computed by numerically diagonalizing H and then performing the infinite-time average exactly using the eigenvalue-grouping algorithm described in Sec. II A.

A. Spin-1/2 chains

Figure 4 shows $\overline{\text{ep}}$ as a function of Δ for spin-1/2 XXZ chains at $L = 4, 6, 8$, and 10 . Three dips at $\Delta = -1, 0$, and 1 are clearly visible for all chain lengths, confirming that the symmetry–entanglement correlation. The most striking feature is the dip at the XX point $\Delta = 0$, which is not present at $L = 2$ in Fig. 2. (This is due to an accidental cancellation at $\Delta = 0$ for the two-site model.) In addition, the depth of the dips at the XXX point decreases rapidly as L increases, while the XX dip remains quite pronounced even at $L = 10$.

The rapid decay of the $SU(2)$ dip with system size has a transparent physical origin. For $L = 2$ the XXX model has only two $SU(2)$ multiplets ($S = 0$ and $S = 1$), and the eigenstates are entirely determined by Clebsch–Gordan coefficients. The symmetry constrains both the eigenvalue degeneracy pattern and the eigenvector structure, producing a large suppression of $\overline{\text{ep}}$.

As L grows, however, the total-spin decomposition $(2s + 1)^{\otimes L} = \bigoplus_S m_S \cdot (2S + 1)$ produces an increasing number of multiplets whose multiplicities m_S grow rapidly. For L spin-1/2 particles, the allowed total-spin values range from $S = 0$ (or $1/2$) to $S = L/2$, so the number of distinct sectors grows only linearly, as $L/2 + 1$. The

multiplicities, on the other hand, must account for the full 2^L -dimensional Hilbert space: $\sum_S m_S (2S + 1) = 2^L$. Since there are only $O(L)$ sectors and the largest dimension $(2S + 1)$ is at most $L + 1$, the dominant multiplicities must grow exponentially to fill the Hilbert space. Indeed, for the singlet sector $m_0 = \binom{L}{L/2} - \binom{L}{L/2+1} \sim 2^L/L^{3/2}$ by Stirling’s approximation.

The $SU(2)$ symmetry labels each eigenstate by its global quantum numbers (S, M) but does not constrain the Hamiltonian dynamics *within* each multiplicity space of dimension m_S . The fraction of the Hilbert space controlled by the symmetry labels is therefore of order $L/2^L$, which vanishes exponentially. Concretely, at $L = 2$ the singlet sector has $m_0 = 1$ —the symmetry completely fixes the eigenstate—while at $L = 10$, $m_0 = 42$, and the Hamiltonian is free to choose among 42 linearly independent singlet states. It is this unconstrained dynamics within the multiplicity spaces that washes out the entanglement suppression.

It is worth emphasizing that the dip does not disappear because the symmetry itself is weakened— $SU(2)$ holds at $\Delta = \pm 1$ for all L —but because the *relative* importance of the symmetry constraint diminishes as the Hilbert space grows exponentially. Numerically, this is demonstrated in Fig. 4 (a) for $L = 10$.

B. XX dip at $\Delta = 0$

In striking contrast to the rapid decay of the XXX dip, the XX dip persists to significantly longer chains. The mechanism is qualitatively different and can be traced to the free-fermion structure at $\Delta = 0$.

The Jordan–Wigner transformation [37, 38] maps spin-1/2 operators to spinless fermion operators c_j, c_j^\dagger via

$$\begin{aligned} S_j^+ &= c_j^\dagger \prod_{l < j} (1 - 2n_l), & S_j^- &= (S_j^+)^{\dagger}, \\ S_j^z &= n_j - \frac{1}{2}, \end{aligned} \quad (31)$$

where $n_j = c_j^\dagger c_j$ is the fermion number operator. For nearest-neighbor sites the Jordan–Wigner string cancels, and the XXZ Hamiltonian (30) becomes [39]

$$H = \sum_{j=1}^{L-1} \left[\frac{1}{2} (c_j^\dagger c_{j+1} + \text{h.c.}) + \Delta (n_j - \frac{1}{2})(n_{j+1} - \frac{1}{2}) \right]. \quad (32)$$

At $\Delta = 0$ the quartic interaction term vanishes and the Hamiltonian reduces to free fermions hopping on a chain of L sites with open boundary conditions. The resulting single-particle energies are $\varepsilon_k = \cos(k\pi/(L + 1))$ for $k = 1, 2, \dots, L$, and each many-body energy eigenvalue is a sum of a subset of these single-particle levels: $E = \sum_{k \in \mathcal{S}} \varepsilon_k$, where \mathcal{S} labels the occupied single-particle states.

The free-fermion structure has a direct consequence for the time-averaged entangling power. The time-averaging

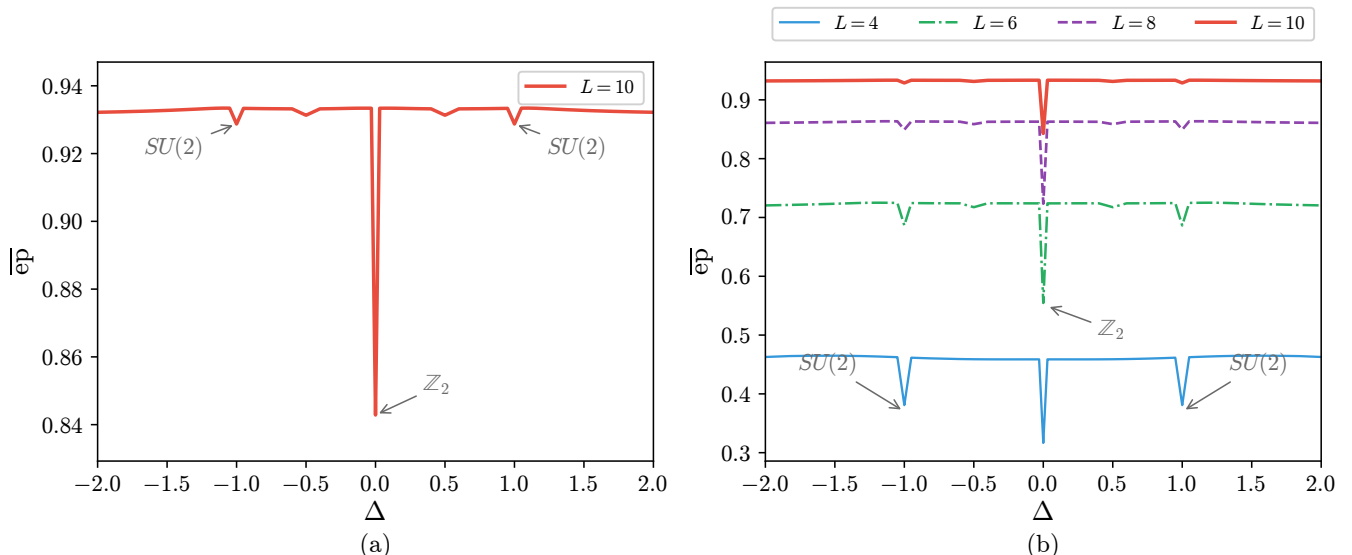


FIG. 4: Time-averaged entangling power $\bar{e}p$ for the spin-1/2 XXZ chain as a function of anisotropy Δ . (a) $L = 10$ chain, shown on a scale to resolve the residual dip structure near saturation. (b) Overlay of $L = 4$ (solid blue), 6 (dash-dotted green), 8 (dashed purple), and 10 (solid red). The $L = 2$ case was already shown in Fig. 2. Root-of-unity fine structure at $\Delta = \pm 1/2$ becomes visible for $L \geq 6$.

algorithm of Sec. II A groups eigenstate pairs by their energy differences: pairs with the same $E_\alpha - E_\beta$ contribute coherently to the purity sums. For a generic interacting Hamiltonian with no special structure, the $d^2 = 4^L$ energy differences $E_\alpha - E_\beta$ are generically all distinct, so nearly every group contains a single pair. Single-pair groups contribute independently to the purity sums—there are no large coherent contributions that could enhance the purity—and the time-averaged entangling power remains close to the Haar-random value. At the free-fermion point the situation is qualitatively different. Since every many-body energy is a sum of single-particle levels ε_k , every energy difference $E_\alpha - E_\beta$ is itself a sum or difference of at most L values drawn from a set of size L . The number of distinct energy differences therefore grows only polynomially, as $O(L^3)$, even though the number of eigenstate pairs grows exponentially as $O(4^L)$. Exponentially many pairs are thus forced into polynomially many groups, creating large degenerate groups whose coherent contributions *can* enhance the purity sums. Whether and by how much these contributions actually suppress $\bar{e}p$ depends on the Hilbert–Schmidt overlaps of the M -matrices within each group—a quantity not determined by the counting argument alone—but the numerical data confirm that the suppression is substantial. Because the polynomial-versus-exponential mismatch persists for all L , the XX dip decays much more slowly than the XXX dip.

The free-fermion structure also explains a second, more subtle feature of the XX dip. The single-particle energies $\varepsilon_k = \cos(k\pi/(L+1))$ satisfy $\varepsilon_k + \varepsilon_{L+1-k} = 0$, so the single-particle spectrum is symmetric about zero. Particle–hole conjugation therefore maps every many-

body eigenvalue E to $-E$, endowing the Hamiltonian with a \mathbb{Z}_2 spectrum-flipping symmetry. In the spin language this symmetry is generated by $W = e^{i\pi S_{z,1}} \otimes I \otimes e^{i\pi S_{z,3}} \otimes I$, the tensor product of the single-site π -rotation of Sec. III B applied to alternating (odd-numbered) sites. The operator W acts on one site from each subsystem, and the $E \leftrightarrow -E$ pairing forces additional spectral degeneracies beyond those already required by the free-fermion group counting, further enhancing the purity sums.

It is illuminating to decompose the entangling power into its two purity sums, \bar{I}_0 and \bar{I}_1 , associated with the transposition operators T_{13} (the A -swap) and T_{24} (the B -swap) in the doubled Hilbert space, respectively. For a symmetric bipartition ($d_A = d_B$), one might expect these two contributions to be comparable. At the XXX point ($\Delta = 1$) this is indeed the case: $SU(2)$ symmetry treats T_{13} and T_{24} on equal footing, producing $\delta\bar{I}_0 = \delta\bar{I}_1$ relative to the generic XXZ values. The $SU(2)$ dip is therefore a *symmetric* enhancement of both purity contributions. At the XX point, however, the particle–hole generator W couples differently to T_{13} than to T_{24} : it acts on sites 1 and 3 (one from A and one from B), breaking the $A \leftrightarrow B$ symmetry. The result is a pronounced asymmetry $\delta\bar{I}_0 \gg \delta\bar{I}_1$ —for $L = 4$, $\delta\bar{I}_0/\delta\bar{I}_1$ is approximately tenfold—driving the deep XX dip.

This asymmetric mechanism is invisible at $L = 2$, where the universal Bell-state eigenvectors cause $\delta\bar{I}_0$ and $\delta\bar{I}_1$ to cancel exactly, producing no net dip. For $L \geq 4$, the eigenvectors become coupling-dependent, the cancellation is broken, and the particle–hole symmetry generates a large, asymmetric enhancement of \bar{I}_0 that grows with L relative to the XXX contribution.

We note that, at $\Delta = 0$, the spin-1/2 XX point also enjoys a non-invertible lattice symmetry implementing T-duality of the compact-boson IR theory [40].² This non-invertible structure is related to the free-fermion integrability exploited above and is special to the Jordan–Wigner algebra of spin-1/2 chains.

C. Quantum Group at Root-of-unity

In addition to the striking dips at $\Delta = 0$ and $\Delta = \pm 1$, fine structure appears at $\Delta = \pm 1/2$ for $L \geq 6$, visible in Fig. 4. These additional features have a purely algebraic origin: they arise from a hidden symmetry that the XXZ model possesses for *all* values of Δ , not only at the XXX point.

At the isotropic point $\Delta = 1$, the XXZ Hamiltonian has $SU(2)$ symmetry and the Hilbert space decomposes into familiar spin- j multiplets. Away from the isotropic point, the full $SU(2)$ is broken, but a deformed version survives. The spin-1/2 XXZ Hamiltonian with open boundary conditions commutes with the generators of $U_q(\mathfrak{sl}_2)$, the quantum group introduced by Drinfel’d [41] and Jimbo [42] as a one-parameter deformation of \mathfrak{sl}_2 , the Lie algebra of $SU(2)$. (See, e.g., Ref. [43, 44] for pedagogical introductions.) The deformation parameter q is related to Δ by

$$\Delta = \cos \gamma, \quad q = e^{i\gamma}, \quad (33)$$

so that $q = 1$ at the XXX point $\Delta = 1$ and $q = i$ at the free-fermion point $\Delta = 0$. Concretely, the deformed algebra is generated by raising and lowering operators J_{\pm} together with an exponentiated Cartan generator $K = q^{J_z}$, satisfying the q -deformed commutation relations

$$KJ_{\pm}K^{-1} = q^{\pm 1}J_{\pm}, \quad [J_+, J_-] = \frac{K^2 - K^{-2}}{q - q^{-1}}. \quad (34)$$

In the limit $q \rightarrow 1$ the right-hand side of the second relation reduces to $2J_z$, recovering the standard \mathfrak{sl}_2 algebra. The key point is that, for generic values of q , the representation theory of $U_q(\mathfrak{sl}_2)$ mirrors that of \mathfrak{sl}_2 : irreducible representations are labeled by non-negative half-integers j , each of dimension $2j + 1$, and the spectrum of the XXZ chain decomposes into $U_q(\mathfrak{sl}_2)$ multiplets in close analogy with the $SU(2)$ case. In this sense the XXZ model retains a “deformed $SU(2)$ ” symmetry for all Δ , which is the algebraic reason underlying its integrability.

The situation changes drastically when q is a root of unity, i.e., when $q^N = 1$ for some positive integer N [45–47]. In ordinary $SU(2)$ representation theory, every representation is either irreducible or decomposes as a direct sum of irreducible representations. At roots of unity, this

familiar structure breaks down: the center of the algebra enlarges, and representations of spin $j \geq N/2$ become *reducible but indecomposable*—they contain invariant subspaces but cannot be split into a direct sum of irreducibles. To illustrate: in ordinary $SU(2)$, if a representation contains a spin- j subspace, one can always find an orthogonal complement that is itself invariant, decomposing the full space as $V_j \oplus V_{j'}$. At roots of unity this complementary subspace does not exist—the action of the generators on vectors outside the invariant subspace necessarily mixes them back in. As a result, multiplets that would form independent irreducible representations at generic q are forced into a single indecomposable block at roots of unity. Since the Hamiltonian commutes with the quantum group generators, it must act as a scalar on each indecomposable block; the previously distinct multiplets are therefore constrained to share the same energy eigenvalue, producing degeneracies that have no counterpart in the ordinary \mathfrak{sl}_2 theory.

To be concrete, consider $\Delta = 1/2$, which corresponds to $\gamma = \pi/3$ and $q = e^{i\pi/3}$, a primitive sixth root of unity ($q^6 = 1$). For a chain of length $L \geq 6$, the Hilbert space is large enough to accommodate representations with $j \geq 3$, and these higher-spin representations become indecomposable. The resulting degeneracies are additional to those already present from $U_q(\mathfrak{sl}_2)$ at generic q : eigenvalues that would be distinct at nearby values of Δ become exactly degenerate at $\Delta = 1/2$. Within the time-averaging framework of Sec. II A, these additional degeneracies enlarge the ω -groups and thereby create the *potential* for further suppression of $\overline{\text{ep}}$; the numerical results below (see Fig. 5) confirm that this potential is realized.

This algebraic picture makes three testable predictions. First, the width of the dip should be extremely narrow, reflecting the fact that the indecomposable structure exists only exactly at the root-of-unity point; any deviation from $q^N = 1$ restores the generic representation theory and lifts the additional degeneracies. Second, the dips should appear symmetrically at $\Delta = \pm 1/2$, because the transformation $\gamma \rightarrow \pi - \gamma$ maps $\Delta \rightarrow -\Delta$ while preserving the root-of-unity condition. Third, the dips should become visible only for $L \geq 6$, since shorter chains do not have representations of sufficiently high spin to trigger the indecomposable structure. A complete analytical prediction for the root-of-unity dip depth would require computing the Hilbert–Schmidt overlaps of M -matrices within each indecomposable block—a nontrivial representation-theoretic calculation that we leave for future work.

To confirm the root-of-unity prediction at higher N and longer chains, we perform a dense scan of Δ values in the interval $[0.25, 0.85]$, with the exact algebraic values $\Delta = 1/2$ ($N = 3$, 6th root), $\Delta = 1/\sqrt{2}$ ($N = 4$, 8th root), $\Delta = \cos(2\pi/5)$ ($N = 5$, 10th root), and $\Delta = \cos(\pi/5)$ ($N = 5$, 10th root) explicitly included in the grid. Fig. 5 shows the results for $L = 10$. All four special points exhibit clear dips centered precisely at the predicted algebraic values. The dip depths follow the expected N -

² We thank Shu-Heng Shao for bringing Ref. [40] to our attention.

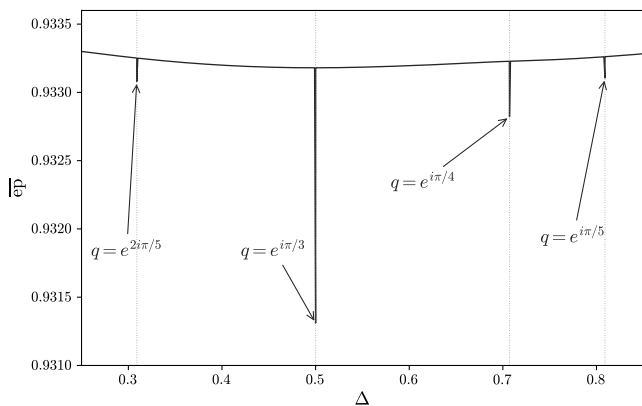


FIG. 5: Dense scan of $\overline{\mathcal{E}}$ for the spin-1/2 XXZ chain at $L = 10$ over $\Delta \in [0.25, 0.85]$, resolving all four root-of-unity dips. Vertical dashed lines mark the exact algebraic locations.

hierarchy: the $N = 3$ dip is the deepest, followed by $N = 4$, while the two $N = 5$ windows produce the shallowest dips. At $L = 8$ the same hierarchy holds with the dips becoming shallower for increasing L .

This decrease of the root-of-unity dip depths with L parallels the behavior of the XXX dip rather than the free-fermion dip: both are driven by symmetry constraints that become subdominant as the Hilbert space dimension grows. The hierarchy in N can be understood from the observation that higher-order roots of unity require representations of higher spin before the indecomposable structure becomes operative, so the corresponding dips need increasingly long chains to develop.

D. Spin-1 chains

We extend the calculation to spin-1 XXZ chains with $L = 2, 4$, and 6 sites. Fig. 6 shows $\overline{\mathcal{E}}$ as a function of Δ for the three chain lengths. The qualitative picture is the same as spin-1/2: three dips at $\Delta = -1, 0$, and 1 persist for all chain lengths studied, and the dip depths decrease as L increases.

Two features distinguish the spin-1 results from spin-1/2. First, the XX dip at $\Delta = 0$ is already visible at $L = 2$, contrary to the $L = 2$, spin-1/2 case. This difference traces back to the two-site eigenvector structure: for spin-1/2, the Bell-state eigenvectors are universal and coupling-independent, producing the exact I_0/I_1 cancellation that renders the XX dip invisible at $L = 2$. For spin-1, the eigenvectors are already coupling-dependent at $L = 2$, so the \mathbb{Z}_2 symmetry at $\Delta = 0$ produces a visible 7% dip even in the minimal model.

Second, and perhaps most strikingly, the *relative* depth of the XX and XXX dips evolves in the opposite direction compared with spin-1/2. For spin-1/2 chains, the free-fermion mechanism at $\Delta = 0$ causes the XX dip to persist and even deepen relative to the XXX dip as L grows: by $L = 10$ the XX dip is more than twice the XXX dip. For

spin-1, the situation is reversed: the XX dip at $\Delta = 0$ decays *faster* than the XXX dip at $\Delta = \pm 1$. The contrast with spin-1/2 can be traced to the absence of a simple free-fermion mapping for the spin-1 chain: the Jordan–Wigner transformation applies only to spin-1/2 systems, so the polynomial-versus-exponential counting argument of Sec. IV B does not carry over. As a result, the XX dip in the spin-1 chain decays at a rate comparable to the XXX dip. More generally, all dips decay faster with L for spin-1 than for spin-1/2. This is expected on general grounds: the larger local Hilbert space ($d_{\text{loc}} = 3$ versus 2) means $d = 3^L$ grows faster than 2^L , and the symmetry constraints become subdominant more rapidly.

V. ENTANGLING POWER AND INTEGRABILITY

The XXZ chain is Bethe-ansatz integrable for all values of Δ , so the symmetry dips documented in Sec. IV are features that appear *within* an integrable family. A natural question is whether the entangling power can also detect integrability, or whether the dips it reveals are purely symmetry-driven. We address this question from two complementary directions. First, we break integrability while preserving the symmetry structure by adding a next-nearest-neighbor coupling (the J_1 - J_2 model). Second, we explore a different integrable family—the bilinear-biquadratic spin-1 chain—that contains an $SU(3)$ -symmetric point and exhibits a qualitatively different degeneracy structure.

A. Integrability breaking via the J_1 - J_2 coupling

Consider the spin-1/2 J_1 - J_2 XXZ chain with open boundary conditions:

$$H = J_1 H_{\text{XXZ}} + J_2 \sum_{j=1}^{L-2} \vec{S}^{(j)} \cdot \vec{S}^{(j+2)}, \quad (35)$$

where H_{XXZ} is the Hamiltonian in Eq. (30). At $J_2 = 0$ the model reduces to the integrable XXZ chain. For $J_2 \neq 0$, integrability is generically broken. We set $J_1 = 1$ throughout.

Figure 7(a) shows $\overline{\mathcal{E}}$ as a function of J_2 at fixed $\Delta = 0.5$ for $L = 8$. A clear dip is visible at $J_2 = 0$: the integrable point has $\overline{\mathcal{E}} \approx 0.859$, approximately 0.5% below the generic non-integrable values ($\overline{\mathcal{E}} \approx 0.863$). Again the dip is very sharp: dense numerical scans with 300 uniformly-spaced J_2 values in $[-0.5, 0.5]$ reveal that at $|J_2| \gtrsim 0.002$ the entangling power has already returned to its generic non-integrable value, and only the *exactly* integrable point $J_2 = 0$ shows any suppression.

Figure 7(b) compares the Δ -dependence of $\overline{\mathcal{E}}$ at $J_2 = 0$ and $J_2 = 0.2$ for $L = 8$. The results reveal a clear hierarchy of robustness among the three dip features: both

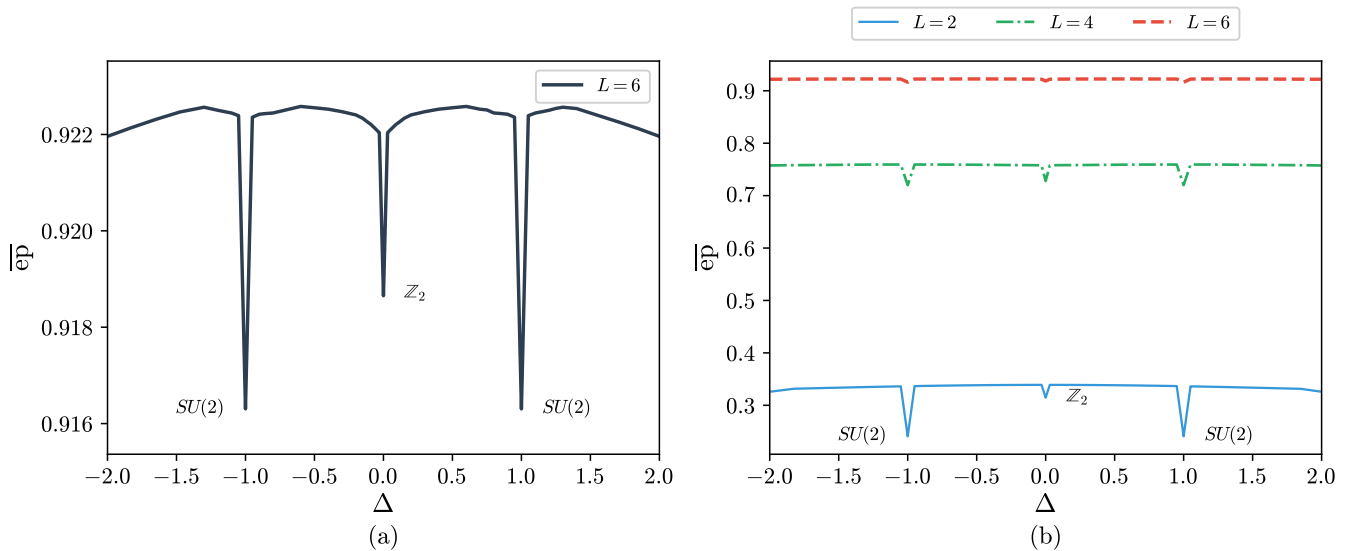


FIG. 6: Time-averaged entangling power \overline{ep} for the spin-1 XXZ chain as a function of anisotropy Δ . (a) Zoom in for $L = 6$. (b) Overlay of $L = 2$ (solid blue), 4 (dash-dotted green), and 6 (dashed red). All three dips at $\Delta = -1, 0$, and 1 are visible but decay rapidly with L .

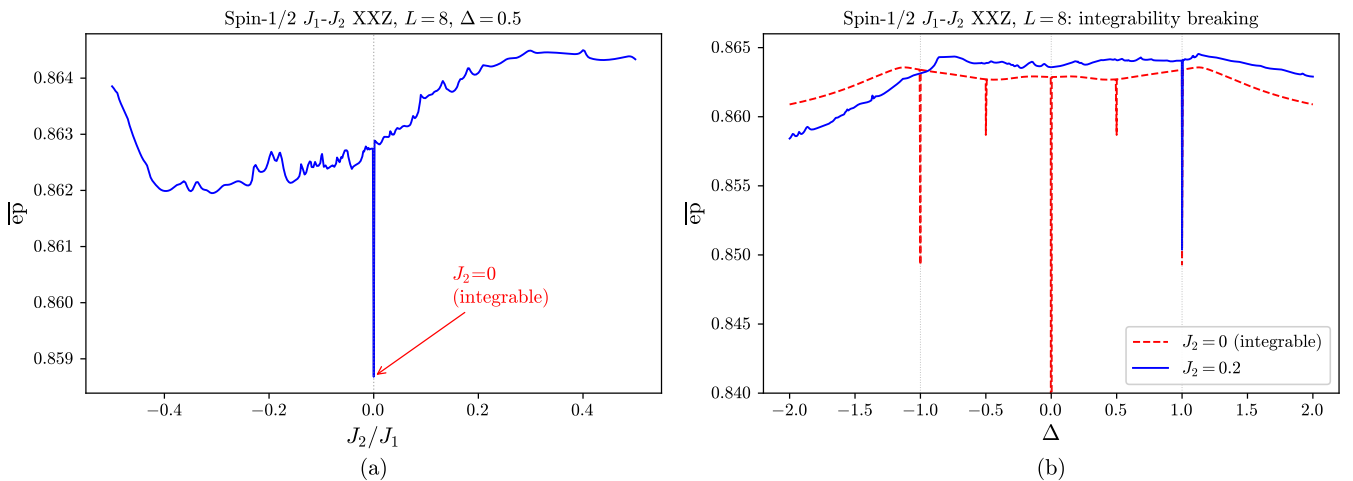


FIG. 7: Time-averaged entangling power for the spin-1/2 J_1 - J_2 XXZ chain at $L = 8$. (a) \overline{ep} as a function of the integrability-breaking parameter J_2/J_1 at fixed $\Delta = 0.5$. A dip at $J_2 = 0$ (the integrable point) is visible, with \overline{ep} approximately 0.5% below the generic non-integrable plateau. (b) \overline{ep} as a function of anisotropy Δ , comparing $J_2 = 0$ (integrable, dashed red) and $J_2 = 0.2$ (non-integrable, solid blue). The symmetry dips at $\Delta = 0$ and $\Delta = -1$ are almost entirely eliminated by the integrability-breaking perturbation, while the XXX dip at $\Delta = 1$ survives.

the XX dip at $\Delta = 0$ and the $\Delta = -1$ dip nearly disappeared for $J_2 = 0.2$, while the XXX dip at $\Delta = 1$ survives and even deepens slightly. The survival of the XXX dip is expected: the isotropic J_1 - J_2 XXX model at $\Delta = 1$ retains full $SU(2)$ symmetry regardless of J_2 , while the surrounding XXZ points still have only $U(1)$. In contrast, the \mathbb{Z}_2 spectrum-flipping symmetry $W = e^{i\pi S_{z,1}} \otimes I \otimes e^{i\pi S_{z,3}} \otimes I$ that generates the XX dip acts on nearest-neighbor pairs and is destroyed by the J_2 coupling.

B. Bilinear-biquadratic spin-1 chain

In this subsection we study the bilinear-biquadratic spin-1 chain, which provides another controlled setting to study the interplay between entangling power and integrability.

The most general isotropic nearest-neighbor spin-1 Hamiltonian (up to an overall scale) can be

parametrized as

$$H = \sum_{j=1}^{L-1} \left[\cos \theta \vec{S}_j \cdot \vec{S}_{j+1} + \sin \theta (\vec{S}_j \cdot \vec{S}_{j+1})^2 \right], \quad (36)$$

where $\theta \in [0, 2\pi)$ parametrizes the ratio of the bilinear and biquadratic couplings. This model has a rich phase diagram [48–50] with several special integrable points: $\theta = 0$ is the isotropic XXX chain, with $SU(2)$ symmetry; $\theta = \pi/4$ is the Uimin–Lai–Sutherland (ULS) point [51–53], at which the bilinear and biquadratic couplings are equal and the symmetry is enhanced from $SU(2)$ to $SU(3)$; $\theta = -\pi/4$ (equivalently $7\pi/4$) is the Takhtajan–Babujian point [54, 55], which is also integrable; and $\theta = \pi/2$ is the pure biquadratic chain.

Figure 8 shows \overline{ep} as a function of θ for chains of length $L = 2, 4$, and 6 . Away from the special points, \overline{ep} forms a high plateau, punctuated by sharp dips at the biquadratic, ULS, and XXX points. The most dramatic feature is the deep dip at the pure biquadratic point $\theta = \pi/2$, at which point the Hamiltonian is purely biquadratic, $H = \sum_j (\vec{S}_j \cdot \vec{S}_{j+1})^2$, and for $L = 2$ the spectrum has the degeneracy pattern $\{1, 1, 1, 1, 1, 1, 4\}$ —whose algebraic origin in the Temperley–Lieb algebra we explain below—which is far more degenerate than the XXX pattern $\{1, 3, 5\}$. This extreme degeneracy suppresses the entangling power by eliminating nearly all oscillatory terms in the time average. In contrast to the biquadratic dip, the ULS point at $\theta = \pi/4$ shows a moderate but clearly visible suppression, while the XXX point at $\theta = 0$ shows much smaller dips.

It is worth pointing out that the Takhtajan–Babujian point at $\theta = -\pi/4$ (equivalently $7\pi/4$) shows no discernible dip at any chain length studied: \overline{ep} at this point is indistinguishable from the generic plateau to within 0.2%. This is a striking result given that the TB point is integrable and solvable by Bethe ansatz, just as the XXX chain. However, the spectrum at $\theta = 7\pi/4$ does not exhibit the enhanced degeneracies that suppress the time-averaged entangling power at the other special points. It would be interesting to study if an entanglement probe exists for the TB point.

Given the strong biquadratic suppression due to the extreme eigenvalue degeneracy at $\theta = \pi/2$, it is worth explaining its algebraic origin. For two spin-1 particles on neighboring sites i and $i+1$, the total spin S_{tot} can be 0, 1, or 2, and the biquadratic interaction can be written as $(\vec{S}_i \cdot \vec{S}_{i+1})^2 = 3P_0^{(i)} + 1$, where $P_0^{(i)}$ is the projector into total spin zero for the neighboring sites. Dropping the additive constant and defining $e_i \equiv 3P_0^{(i)}$, the pure biquadratic Hamiltonian takes the form $H = \sum_i e_i$. The generators e_i so defined satisfy three relations: $e_i^2 = \delta e_i$ with $\delta = 2s + 1$ (equal to 3 for spin-1, since $e_i^2 = 9P_0 = 3e_i$), $e_i e_{i\pm 1} e_i = e_i$ (the braid-like relation that couples neighboring bonds), and $[e_i, e_j] = 0$ for $|i-j| \geq 2$ (locality). These are the defining relations of the Temperley–Lieb (TL) algebra [56], with loop fugacity $\delta = 3$.

The TL algebra endows the biquadratic chain with both a symmetry structure and integrability. On the symmetry side, because the Hamiltonian is built entirely from TL generators, the TL algebra—rather than $SU(2)$ —is the relevant algebraic structure organizing the spectrum. The TL algebra is also intimately connected to the quantum group $U_q(sl_2)$ via $q + q^{-1} = \delta$ [43, 45], linking it to the root-of-unity discussion in Sec. IV C, although here q is real and the representation theory remains semisimple. On the integrability side, from the TL generators one can construct an R -matrix satisfying the Yang–Baxter equation, making the pure biquadratic chain exactly solvable by Bethe ansatz [57, 58].

The contrast with the Takhtajan–Babujian point is instructive: both $\theta = \pi/2$ and $\theta = -\pi/4$ are integrable and Bethe-ansatz solvable [54, 55, 57], yet only the biquadratic point exhibits a dip in \overline{ep} . The crucial difference lies in the spectral degeneracy pattern imposed by the TL algebra. The Hilbert space $(\mathbb{C}^3)^{\otimes L}$ decomposes into irreducible TL modules whose dimensions are determined by Chebyshev polynomials of the second kind evaluated at $\delta/2$ [59]. Concretely, for $L = 2$ the TL decomposition yields the degeneracy pattern $\{1, 1, 1, 1, 1, 1, 4\}$ noted above—eight singlet blocks and one four-dimensional block—which is far more fragmented than the $SU(2)$ pattern $\{1, 3, 5\}$. For larger L the disparity grows rapidly: the TL modules produce degenerate blocks that are much larger than those of the standard $SU(2)$ or $SU(3)$ multiplet decompositions. It is this extreme TL degeneracy, rather than integrability or any continuous symmetry, that drives the strong suppression of \overline{ep} at the biquadratic point.

VI. THERMODYNAMIC LIMIT: QUASI-PARTICLE SCATTERINGS

The results of the preceding sections demonstrate that the many-body \overline{ep} is a sensitive probe of symmetry-induced spectral degeneracies in finite systems. Integrability can amplify these degeneracies—as at the free-fermion and root-of-unity points—but need not do so: the Takhtajan–Babujian point is Bethe-ansatz integrable yet produces no discernible dip. The entangling power therefore detects algebraic structure that manifests as enhanced degeneracies, regardless of whether that structure originates from a continuous symmetry, a quantum group, or the Temperley–Lieb algebra.

It is then natural that the signals in the entangling power decay with system size—the Hilbert-space dimension grows exponentially with L , while the number of constraints grows only polynomially, so their relative weight is progressively diluted. Far from being a shortcoming, this vanishing is a reflection of the fact that \overline{ep} probes the global structure of the *entire* spectrum and its eigenvectors, a structure that becomes increasingly dominated by generic, symmetry-agnostic features as the system grows.

To construct a diagnostic that survives the thermo-

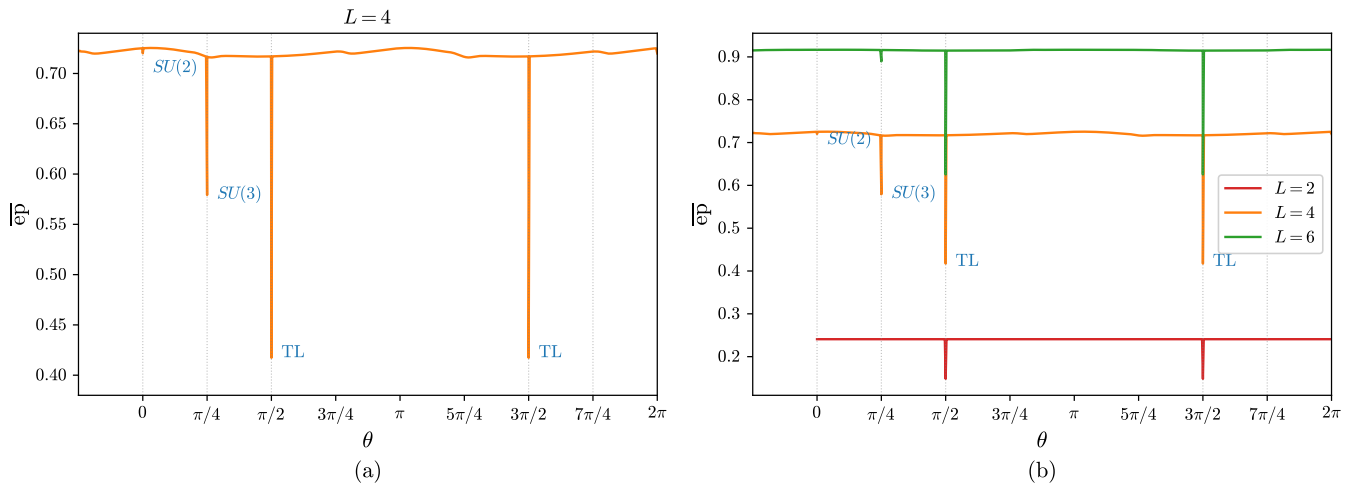


FIG. 8: Time-averaged entangling power $\bar{e}p$ for the bilinear-biquadratic spin-1 chain (36) as a function of θ . (a) $L = 4$, where the full dip hierarchy is most clearly resolved: Temperley–Lieb (TL , $\theta = \pi/2, 3\pi/2$), $SU(3)$ ($\theta = \pi/4$), and $SU(2)$ ($\theta = 0$). (b) Overlay of $L = 2$ (red), $L = 4$ (orange), and $L = 6$ (green).

dynamic limit, we must therefore shift focus from the full many-body spectrum to the low-lying excitations whose structure is most tightly constrained by symmetry. The idea that quasi-particle degrees of freedom provide the natural language for entanglement in the thermodynamic limit has a distinguished pedigree: Calabrese and Cardy showed that the entanglement entropy of a one-dimensional quantum system after a global quench can be understood in terms of entangled quasi-particle pairs propagating ballistically from the initial state [15, 16, 60]. In their picture, quasi-particles are the *carriers* of entanglement across the system. Here we apply a complementary philosophy: rather than asking how quasi-particles propagate pre-existing entanglement, we ask how much entanglement is *generated* by the dynamics of quasi-particles, which should inherit the dynamics of the underlying spin-chains.

This viewpoint is closely related to the philosophy of effective field theory: the full many-body Hilbert space, with its exponentially growing dimension, plays the role of the UV theory, while the quasi-particle description provides the low-energy effective theory whose dynamics are governed by the symmetries of the underlying system.

Concretely, it is worth recalling that the correlation between entanglement suppression and symmetry enhancement was first discovered in $2 \rightarrow 2$ scattering amplitudes in particle and nuclear physics [1, 2], where the S -matrix is the fundamental observable. Two-magnon scattering is the spin-chain counterpart of this setting: magnons are the elementary excitations, their pairwise S -matrix is fixed by the Yang–Baxter equation, and its entangling power provides an intensive, per-scattering-event diagnostic of symmetry that persists as $L \rightarrow \infty$. In this way, the quasi-particle picture brings the many-body problem back into contact with the scattering framework in which the entanglement–symmetry connection was orig-

inally identified.

A. Two-magnon S -matrix

We now switch from open to periodic boundary conditions, replacing the sum in Eq. (30) by $\sum_{j=1}^L$ with $\vec{S}_{L+1} \equiv \vec{S}_1$. The periodic XXZ Hamiltonian is exactly solvable by the coordinate Bethe ansatz [36, 61–63]. (The finite-size calculations of Secs. IV and V employed open boundary conditions, which are natural for the quantum group analysis; the Bethe ansatz, by contrast, requires translational invariance.) The basic idea is simple: one works in the sector of fixed total S^z and writes an ansatz for the wavefunction as a superposition of plane waves, one for each ordering of the flipped spins. Consider the ferromagnetic vacuum $|\Omega\rangle = |\uparrow\uparrow\cdots\uparrow\rangle$, the state with all spins aligned. Spin-flip excitations above this vacuum are called magnons. A single magnon is created by flipping one spin: acting with S_n^- on site n produces a localized excitation $|n\rangle = S_n^-|\Omega\rangle$. In the Bethe ansatz, the one-magnon eigenstate is a Bloch wave, $|p\rangle = \sum_{n=1}^L e^{ipn} |n\rangle$, carrying quasi-momentum p and spin $\Delta S^z = -1$, with dispersion relation $\epsilon(p) = \Delta - \cos p$. (A self-contained derivation is given in Appendix D.) A single magnon thus propagates freely; when two magnons meet on adjacent sites, however, the wavefunction acquires a phase shift. This phase shift depends on the anisotropy Δ and on the *rapidity* difference of the two magnons. The rapidity is a reparametrization of the quasi-momentum that linearizes the scattering phase—it plays the same role here as the rapidity variable in relativistic kinematics, trading a complicated dependence on momenta for a simple dependence on their difference.

The two-magnon scattering is encoded in the R -

matrix, which is the scattering amplitude in spin and rapidity space: it maps an incoming two-magnon spin state to an outgoing one as a function of the rapidity difference. Since the XXZ Hamiltonian conserves total S^z , the scattering cannot change the total spin projection of the two magnons. Written in the basis $\{|\uparrow\uparrow\rangle, |\uparrow\downarrow\rangle, |\downarrow\uparrow\rangle, |\downarrow\downarrow\rangle\}$, this means that any process connecting states with different total S^z —such as $|\uparrow\uparrow\rangle \rightarrow |\uparrow\downarrow\rangle$ —has vanishing amplitude. Of the sixteen entries, only six survive, giving rise to the so-called six-vertex form [39, 64, 65]:

$$R(u, \gamma) = \begin{pmatrix} a & 0 & 0 & 0 \\ 0 & b & c & 0 \\ 0 & c & b & 0 \\ 0 & 0 & 0 & a \end{pmatrix}, \quad (37)$$

with vertex weights $a = \sin(u + \gamma)$, $b = \sin u$, $c = \sin \gamma$, and $\Delta = \cos \gamma$ [65]. Here u is the spectral parameter encoding the rapidity difference—it is related to the quasi-momentum p of each magnon by $e^{ip} = \sin(u + \gamma/2)/\sin(u - \gamma/2)$ (see Appendix D 4 for details)—and γ is the crossing parameter fixed by the anisotropy. The three types of nonzero entries correspond to the three allowed scattering processes: a is the amplitude for two magnons with the same spin to pass through each other unchanged ($S^z = \pm 1$ sectors), b is the amplitude for opposite-spin magnons to transmit without exchanging spin, and c is the spin-exchange amplitude—the process $|\uparrow\downarrow\rangle \leftrightarrow |\downarrow\uparrow\rangle$. It is the spin-exchange amplitude c that generates entanglement; when $c = 0$ the R -matrix is diagonal and no entanglement is produced.

A key consequence of integrability is that the two-magnon scattering is purely elastic—the magnons emerge with their momenta unchanged, picking up only a phase—and that the multi-magnon S -matrix factorizes into a product of pairwise two-body scatterings [66]. The self-consistency of this factorization is guaranteed by the Yang–Baxter equation [65, 67, 68],

$$R_{12}(u_{12}) R_{13}(u_{13}) R_{23}(u_{23}) = R_{23}(u_{23}) R_{13}(u_{13}) R_{12}(u_{12}), \quad (38)$$

where u_i is the rapidity of magnon i , $u_{ij} \equiv u_i - u_j$, and R_{jk} denotes the R -matrix of Eq. (37) acting on magnons j and k . The crossing parameter γ is common to all R -matrices in the chain, so it is suppressed; only the rapidity difference u_{ij} varies from factor to factor. Eq. (38) is a matrix identity in $\mathbb{C}^2 \otimes \mathbb{C}^2 \otimes \mathbb{C}^2$: it states that the outcome of a three-magnon collision is independent of the order in which the pairwise scatterings are performed—the hallmark of an integrable system.

The R -matrix as written above encodes the relative scattering amplitudes but is not yet a proper S -matrix, because it is not unitary—the outgoing probabilities do not sum to one. This is an artifact of the parametrization: the spectral parameter u is natural in the algebraic setting of the vertex model, but physical scattering corresponds to real rapidity difference θ , related by $u = i\theta$.

Making this substitution and dividing by an overall normalization $\rho = \sqrt{\sin^2 \gamma + \sinh^2 \theta}$ to enforce unitarity, we obtain the physical S -matrix, $S(\theta, \gamma) = R(i\theta, \gamma)/\rho$, which is unitary by construction and describes the physical scattering of two magnons (see Appendix D for details).

B. Entangling power of the S -matrix

Since $S(\theta, \gamma)$ conserves total S^z , its action on $\mathbb{C}^2 \otimes \mathbb{C}^2$ decomposes into three sectors. In the $S^z = \pm 1$ sectors ($|\uparrow\uparrow\rangle$ and $|\downarrow\downarrow\rangle$), no spin exchange is possible and the S -matrix acts as a phase: $S = e^{i\varphi_{\pm}}$. In the $S^z = 0$ sector, spanned by $|\uparrow\downarrow\rangle$ and $|\downarrow\uparrow\rangle$, the 2×2 block has two eigenvalues corresponding to the triplet ($e^{i\varphi_t}$, symmetric) and singlet ($e^{i\varphi_s}$, antisymmetric) channels. Explicitly, the three phases are

$$\begin{aligned} e^{i\varphi_+} &= a/\rho, \\ e^{i\varphi_t} &= (b+c)/\rho, \\ e^{i\varphi_s} &= (b-c)/\rho, \end{aligned} \quad (39)$$

where, after the analytic continuation $u = i\theta$ to physical rapidity,

$$\begin{aligned} a &= \sin \gamma \cosh \theta + i \cos \gamma \sinh \theta, \\ b &= i \sinh \theta, \quad c = \sin \gamma, \end{aligned} \quad (40)$$

with $\rho = \sqrt{\sin^2 \gamma + \sinh^2 \theta}$ and $\Delta = \cos \gamma$.

At fixed rapidity θ , the S -matrix is a finite-dimensional unitary on the spin Hilbert space $\mathbb{C}^2 \otimes \mathbb{C}^2$ —the rapidity enters as a continuous parameter. In the spin-subspace the entangling power of $S(\theta, \gamma)$ is therefore that of a two-qubit gate, and it depends only on the eigenvalue phases. For the S^z -conserving structure above, the overall phase φ_+ drops out, and ep is a function of the two phase differences $\delta_{t+} \equiv \varphi_t - \varphi_+$ and $\delta_{s+} \equiv \varphi_s - \varphi_+$ alone.

To derive the explicit formula, we note that for two qubits ($d_A = d_B = 2$) the linear entropy simplifies to $1 - \text{Tr}(\rho_A^2) = 2 \det \rho_A$, so the entangling power in Eq. (1) reduces to a Haar average of the determinant of the reduced density matrix over random product input states. We parametrize the two input states on their respective Bloch spheres, exploiting the $U(1)$ symmetry to fix one azimuthal angle.

Analytically, the key simplification is that the S -matrix conserves S^z and therefore has only a transmission amplitude B and a spin-exchange amplitude C in the $S^z = 0$ sector, with $|B|^2 + |C|^2 = 1$. When computing $|\det \rho_A|^2$ and integrating over the remaining azimuthal angle, all cross-terms between B and C contain oscillating phases and vanish, leaving two decoupled contributions that can be evaluated in closed form (see Appendix D for the detailed derivation). The result is

$$\begin{aligned} \text{ep}(\delta_{t+}, \delta_{s+}) &= \frac{1}{9} [3 - 2 \cos(\delta_{t+} + \delta_{s+}) \cos(\delta_{t+} - \delta_{s+}) \\ &\quad - \cos^2(\delta_{t+} - \delta_{s+})]. \end{aligned} \quad (41)$$

Eq. (41) is the central formula of this section: it expresses the entanglement power of any S^z -conserving two-qubit unitary entirely in terms of two phase differences, with no reference to the specific dynamical model that produced them.

C. Entanglement and Symmetry

It is instructive to decompose the S -matrix in terms of quantum logic gates. By direct inspection one can write

$$S(\theta, \gamma) = \frac{1}{2}(a+b-c)I + c\text{SWAP} + \frac{1}{2}(a-b-c)\sigma_z \otimes \sigma_z, \quad (42)$$

which is the $U(1)$ generalization of the two-gate decomposition in Ref. [2]. Under $SU(2)$ invariance, $\sigma_z \otimes \sigma_z$ is forbidden and the third term must vanish, giving $a = b+c$ and $S = bI + c\text{SWAP}$, recovering the nucleon-nucleon result. The $\sigma_z \otimes \sigma_z$ coefficient $\frac{1}{2}(a-b-c)$ measures the departure from $SU(2)$: it reflects the anisotropy-induced splitting of the triplet eigenvalues ($\varphi_+ \neq \varphi_t$), permitted by the reduced $U(1)$ symmetry of the XXZ chain.

The key insight from Ref. [2] is that the Identity and the SWAP are the *only* two equivalence classes of two-qubit gates with vanishing entanglement power [69, 70]. (Here $\sigma_z \otimes \sigma_z$ is a product of local unitaries and hence belongs to the Identity class.) In the (θ, Δ) plane, $\text{ep} = 0$ therefore requires S to be locally equivalent to one of these two gates. From Eq. (42), this happens in exactly two regimes:

(i) *$SU(2)$ points* ($\Delta = \pm 1$, all θ). The spin-exchange amplitude vanishes, $c = \sin \gamma = 0$, and one can verify from Eq. (40) that $a = b$ at $\gamma = 0$ and $a = -b$ at $\gamma = \pi$. In both cases only a single term in Eq. (42) survives—proportional to I or to $\sigma_z \otimes \sigma_z$ —and the S -matrix belongs to the Identity class for *all* θ . The rapidity independence has a simple physical origin: at the $SU(2)$ point the S -matrix acts trivially on spin, so the outgoing two-magnon state is an unentangled product state of spin and momentum regardless of the scattering energy. This is the spin-chain counterpart of the entanglement suppression found at the Wigner $SU(4)$ point in nucleon-nucleon scattering, where the S -matrix in the spin-subspace is again an Identity, independent of the centre-of-mass momentum [2].

(ii) *Zero rapidity* ($\theta = 0$, $\Delta \neq \pm 1$). At zero relative momentum $a = c = \sin \gamma$ and $b = 0$, so $S \propto \text{SWAP}$: the two magnons exchange their spin quantum numbers completely. Since SWAP is the other non-entangling gate, $\text{ep} = 0$ here as well, but for a different reason—SWAP rather than Identity.

Away from these two regimes, all three terms in Eq. (42) contribute, the S -matrix belongs to neither non-entangling class, and $\text{ep} > 0$. As the rapidity increases from zero, S interpolates away from the SWAP gate and entanglement is generated. At fixed θ , smaller $|\Delta|$ corresponds to a larger spin-exchange amplitude $c = \sqrt{1 - \Delta^2}$, and hence larger ep . The maximum is achieved at the free-fermion point $\Delta = 0$ ($c = 1$), where the S -matrix has

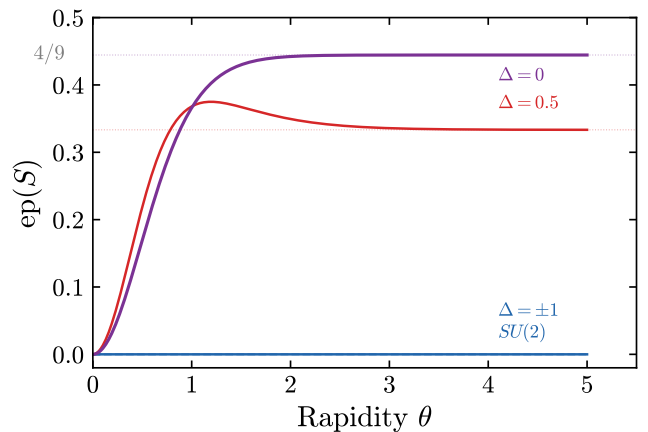


FIG. 9: Entangling power of the two-magnon S -matrix as a function of rapidity θ for several values of the anisotropy Δ . At the $SU(2)$ points $\Delta = \pm 1$, S belongs to the Identity class and $\text{ep} = 0$ for all θ (selection rule). For $\Delta \neq \pm 1$, ep rises from zero ($S \propto \text{SWAP}$ at $\theta = 0$) and approaches the asymptotic value $\text{ep}_\infty = \frac{4}{9}(1 - \Delta^2)$ (dotted lines). The free-fermion point $\Delta = 0$ achieves the maximum at every θ .

maximal spin exchange and ep approaches the two-qubit ceiling $4/9$ at large rapidity (Fig. 9). It is worth pointing out the contrast with the full-spectrum results of the previous sections, where $\Delta = 0$ corresponded to a sharp *dip* in entangling power: there, the free-fermion structure simplified the many-body eigenstates and suppressed entanglement across the full Hilbert space, whereas the quasi-particle S -matrix at $\Delta = 0$ has the *largest* spin-exchange amplitude and is therefore the most entangling. These are complementary perspectives—the full spectrum probes the global structure of the Hilbert space, while the S -matrix isolates the local two-body interaction. It is also worth noting that entanglement suppression is not the only correlation between entanglement and symmetry: in the two-Higgs-doublet model, Ref. [7] showed that *maximizing* the entanglement in Higgs boson scattering also results in enhanced symmetry, providing a complementary example where enhanced symmetry seems to correspond to the extremum in the entanglement, instead of just the minimum.

In the large-rapidity limit $\sinh \theta \gg \sin \gamma$, both phase differences approach the same value, $\delta_{t+}, \delta_{s+} \rightarrow \gamma$, and the S -matrix reduces to the Ising-type ZZ rotation $e^{-i\gamma \sigma_z \otimes \sigma_z / 2}$. Eq. (41) then gives the asymptotic entangling power

$$\text{ep}_\infty(\gamma) = \frac{4}{9} \sin^2 \gamma = \frac{4}{9} (1 - \Delta^2), \quad (43)$$

which provides a simple closed-form expression for the dotted asymptotes in Fig. 9.

VII. CONCLUSIONS

In this work we have undertaken a systematic study of the entangling power of spin-chain Hamiltonians, encompassing two-site models, finite-size chains, and the two-magnon scattering matrix. The central finding is that the correlation between entanglement suppression and symmetry enhancement, previously observed in particle and nuclear physics, extends to spin-chain systems across all settings we have studied.

The exact solution of the two-site models yields an insight that is invisible in $2 \rightarrow 2$ scattering amplitudes in particle and nuclear physics [1, 2]: the time-averaged entangling power depends on *both* the eigenvalue spectrum and the eigenvector structure of the Hamiltonian. For spin-1/2, the eigenvectors are universal Bell states independent of the couplings, so \overline{ep} is determined entirely by the eigenvalue degeneracy pattern—the count N_0 of vanishing frequencies suffices. For spin-1, the eigenvectors become coupling-dependent, and the isospectral analysis reveals that the eigenvector contribution to the suppression at the XXX point is comparable in magnitude to the eigenvalue contribution. This dual mechanism—eigenvalue degeneracy and eigenvector constraint—is a structural feature of many-body Hamiltonians that has no counterpart in the S -matrix, where only eigenvalue phases enter the entangling power. We established the monotonic hierarchy $\overline{ep}_{XYZ} > \overline{ep}_{XXZ} \geq \overline{ep}_{XX} > \overline{ep}_{\text{Ising}} > \overline{ep}_{XXX}$ for both spin-1/2 and spin-1.

For finite-size systems, the symmetry dip persists but its relative depth decays with increasing L . This is not a shortcoming of the entangling power but a reflection of the fact that it probes the *entire* eigenspace—all d^4 quartets of eigenstates contribute to the time-averaged purity sums. As L grows, the Hilbert space dimension d grows exponentially while the number of symmetry-imposed constraints grows only polynomially; the symmetry signal is progressively diluted. Meanwhile, the free-fermion dip at $\Delta = 0$ decays much more slowly, driven by the additivity of the Jordan–Wigner spectrum—a mechanism invisible to any finite-body scattering amplitude. Integrability breaking via a J_2 coupling confirms that symmetry, not integrability, is the driver of the $SU(2)$ suppression. The bilinear-biquadratic spin-1 chain provides a complementary lesson: the $SU(3)$ -symmetric ULS point produces less pronounced suppression than the biquadratic point, while the pure biquadratic point—whose extreme Temperley–Lieb degeneracy far exceeds the $SU(2)$ or $SU(3)$ multiplet structure—hosts the deepest dip of any model we have studied. This confirms that it is the detailed spectral degeneracy pattern, not merely the dimension of the symmetry group, that controls the suppression of \overline{ep} . We note that for the free-fermion and root-of-unity dipoles, the mechanism—polynomial growth of distinct energy differences and indecomposable quantum-group representations, respectively—identifies *why* large ω -groups form, but the quantitative dip depths are established numeri-

cally rather than analytically; closing this gap is an interesting open problem.

That the many-body entangling power fades with system size points naturally to the correct diagnostic in the thermodynamic limit: the dynamics of quasi-particles. Two-magnon scattering is the spin-chain counterpart of $2 \rightarrow 2$ scattering in particle physics, and its entangling power is an intensive, per-scattering-event quantity that persists as $L \rightarrow \infty$. We showed that the S -matrix decomposes into three quantum logic gates—Identity, SWAP, and $\sigma_z \otimes \sigma_z$ —generalizing the $SU(2)$ two-gate decomposition of Ref. [2] to the $U(1)$ -symmetric XXZ chain. The key insight, also from Ref. [2], is that Identity and SWAP are the *only* non-entangling two-qubit gates. The entangling power of the S -matrix therefore vanishes if and only if it belongs to one of these two classes, which occurs at the $SU(2)$ points $\Delta = \pm 1$ for all scattering energies. The free-fermion point $\Delta = 0$ achieves the maximum entangling power at every rapidity, in striking contrast to the full-spectrum result where it corresponds to a sharp dip—illustrating that the S -matrix and the many-body spectrum probe complementary aspects of entanglement.

Taken together, these results trace a single thread across three regimes connected by very different physics: suppressed entangling power at points of enhanced algebraic structure, from microscopic quantum gates through finite-size many-body spectra to asymptotic two-body scattering. That the correlation persists across regimes—and is driven in each case by the spectral degeneracies and eigenvector constraints imposed by the symmetry—suggests it is a robust organizing principle rather than an artifact of any single setting.

It is worth pointing out that the finite-size entanglement power is directly relevant to near-term quantum platforms. Programmable quantum simulators based on cold atoms, trapped ions, or superconducting qubits [71–73] now routinely realize spin chains with tunable anisotropy in the range of system sizes we have studied ($L = 4$ – 10). The dip structure of the time-averaged entangling power as a function of the anisotropy parameter could serve as a symmetry witness: one prepares random product states, evolves under the implemented Hamiltonian, and measures the average entanglement produced. A key advantage of this protocol is that it probes the symmetry content of the dynamics itself, without requiring the preparation of a specific eigenstate or *a priori* knowledge of the conserved charges. This distinguishes it from state-based diagnostics such as ground-state entanglement entropy or symmetry-resolved entanglement, which presuppose both. Deviations from the predicted dip pattern would signal that hardware noise or calibration errors have broken the intended symmetry of the simulation. More broadly, the entangling power generalizes the standard two-qubit gate characterization to multi-qubit unitaries, which is of interest for benchmarking entangling blocks in quantum circuit design.

Several directions for future work suggest themselves. A quantitative connection between the S -matrixentan-

gling power and the many-body dip depth remains to be established. It would also be interesting to extend the gate decomposition to higher-rank models ($d = 3$ and beyond) where the R -matrix is known. Finally, spectral correlations beyond the entanglement power—such as the cross spectral form factor introduced in Ref. [74] for bootstrapping hidden symmetries from level statistics—offer a complementary route to diagnosing symmetry and integrability in many-body systems, and understanding the interplay between these spectral approaches remains an open challenge.

Acknowledgments

We thank Daniel Arovas, Jens Koch and Shu-Heng Shao for discussions. This work is supported in part by the U.S. Department of Energy under contracts No. DE-SC0023522, No. DE-SC0010143, and No. 89243024CSC000002 (QuantISED Program). This research was supported in part through the computational resources and staff contributions provided for the Quest high performance computing facility at Northwestern University which is jointly supported by the Office of the Provost, the Office for Research, and Northwestern University Information Technology.

The AI assistant Claude (Anthropic) was used during this work for code implementation and manuscript preparation. Code used in this work was produced with AI assistance under close human supervision and was validated against known analytical results and internal consistency tests. The authors originated the scientific ideas and direction of the work, developed the physical insights and logical flow of the paper, and extensively revised, restructured, and finalized the manuscript text. The authors take full responsibility for the accuracy, originality, and integrity of the work, and no AI tool is listed as an author.

Appendix A: Derivation of the time-averaging algorithm in Section II A

In this appendix we derive the algorithm presented in Sec. II for computing the time-averaged entangling power $\overline{\text{ep}}$. Throughout we specialize to the equal bipartition $d_A = d_B \equiv d$, which is the case relevant for the spin-chain calculations in this work. The starting point is the operator formula (3), which we write for $\alpha = 0$ as

$$I_0(U) = \text{Tr}(T_{13}) + \text{Tr}[(U^\dagger)^{\otimes 2} T_{13} U^{\otimes 2} T_{13}]. \quad (\text{A1})$$

For a time-independent Hamiltonian, $U(t) = e^{iHt} = \sum_n e^{iE_n t} |n\rangle\langle n|$, and in the doubled Hilbert space $(\mathcal{H}_A \otimes \mathcal{H}_B)^{\otimes 2}$ we have $U^{\otimes 2}(t) = \sum_{k,l} e^{i(E_k + E_l)t} |kl\rangle\langle kl|$, where $|kl\rangle \equiv |k\rangle_1 \otimes |l\rangle_2$ labels the energy eigenstates in the first

and second copies. Inserting this into Eq. (A1) and using $T_{13}^\dagger = T_{13}$, we obtain

$$\begin{aligned} I_0^{(2)}(t) &\equiv \text{Tr}[(U^\dagger)^{\otimes 2} T_{13} U^{\otimes 2} T_{13}] \\ &= \sum_{k,l,m,n} e^{i(E_k + E_l - E_m - E_n)t} \\ &\quad \times |\langle kl|T_{13}|mn\rangle|^2. \end{aligned} \quad (\text{A2})$$

The modulus squared arises because T_{13} is Hermitian and appears on both sides of $U^{\otimes 2}$: $\langle mn|T_{13}|kl\rangle = (\langle kl|T_{13}|mn\rangle)^*$.

1. Matrix element of the swap operator

We now evaluate $\langle kl|T_{13}|mn\rangle$ in the product basis. Let $\{|a\rangle\}$ and $\{|b\rangle\}$ be orthonormal bases for \mathcal{H}_A and \mathcal{H}_B , respectively. Each eigenvector decomposes as $|n\rangle = \sum_{a,b} (C_n)_{ab} |a\rangle \otimes |b\rangle$, where C_n is a $d_A \times d_B$ matrix. In the doubled space the basis is $|a_1, b_1, a_2, b_2\rangle$, with positions 1 and 2 labelling the A -factor and the B -factor of each copy. The swap operator T_{13} exchanges the two A -factors:

$$T_{13} |a_1, b_1, a_2, b_2\rangle = |a_2, b_1, a_1, b_2\rangle. \quad (\text{A3})$$

Therefore

$$\begin{aligned} &\langle kl|T_{13}|mn\rangle \\ &= \sum_{a,b,c,d} (C_k)_{cb}^* (C_l)_{ad}^* (C_m)_{ab} (C_n)_{cd} \\ &= \sum_{a,c} \left(\sum_b (C_m)_{ab} (C_k^\dagger)_{bc} \right) \\ &\quad \times \left(\sum_d (C_n)_{cd} (C_l^\dagger)_{da} \right) \\ &= \text{Tr}_A(C_m C_k^\dagger \cdot C_n C_l^\dagger). \end{aligned} \quad (\text{A4})$$

In the first line we expanded $|mn\rangle$ and $\langle kl|$, applied T_{13} (which sends $a_1 \rightarrow a_2$ and $a_2 \rightarrow a_1$), and contracted the indices. The second line collects the sums over b and d into matrix products, yielding the trace over \mathcal{H}_A of two $d_A \times d_A$ matrices.

2. Time average and eigenvalue grouping

The infinite-time average of Eq. (A2) retains only those quartets (k, l, m, n) satisfying $E_k + E_l = E_m + E_n$, or equivalently $E_k - E_m = E_n - E_l \equiv \omega$:

$$\begin{aligned} \overline{I_0^{(2)}} &= \sum_{\omega} \sum_{\substack{(k,m): E_k - E_m = \omega \\ (n,l): E_n - E_l = \omega}} \\ &\quad \times |\text{Tr}_A(C_m C_k^\dagger \cdot C_n C_l^\dagger)|^2. \end{aligned} \quad (\text{A5})$$

For each value of ω , define a group g_ω consisting of all pairs of eigenstates (p, q) with $E_p - E_q = \omega$, and label them $i = 1, 2, \dots, N_\omega$. For the i th pair (p_i, q_i) , define the $d_A \times d_A$ matrix

$$M_i \equiv C_{p_i} C_{q_i}^\dagger. \quad (\text{A6})$$

Using Eq. (A4), the matrix element becomes $\text{Tr}_A(C_m C_k^\dagger \cdot C_n C_l^\dagger) = \text{Tr}_A(M_i^\dagger M_j)$ where i labels the pair (k, m) and j labels the pair (n, l) , both belonging to the same group g_ω . Equation (A5) then takes the compact form

$$\overline{I_0^{(2)}} = \sum_\omega \sum_{i,j=1}^{N_\omega} |\text{Tr}_A(M_i^\dagger M_j)|^2. \quad (\text{A7})$$

3. Relation between I_1 and I_0

The formula for $\alpha = 1$ reads

$$I_1(U) = \text{Tr}(T_{24}) + \text{Tr}[(U^\dagger)^{\otimes 2} T_{24} U^{\otimes 2} T_{13}]. \quad (\text{A8})$$

Unlike I_0 , the two swap operators flanking $U^{\otimes 2}$ are different (T_{24} and T_{13}), so the $|\cdot|^2$ factorization of Eq. (A2) does not apply directly. Instead, we relate $I_1(U)$ to I_0 evaluated on a modified unitary.

Let S denote the SWAP gate on $\mathcal{H}_A \otimes \mathcal{H}_B$, i.e. $S|a, b\rangle = |b, a\rangle$. We claim that $S^{\otimes 2} T_{13} S^{\otimes 2} = T_{24}$. This is verified by acting on a basis vector:

$$\begin{aligned} |a_1, b_1, a_2, b_2\rangle &\xrightarrow{S^{\otimes 2}} |b_1, a_1, b_2, a_2\rangle \\ &\xrightarrow{T_{13}} |b_2, a_1, b_1, a_2\rangle \xrightarrow{S^{\otimes 2}} |a_1, b_2, a_2, b_1\rangle, \end{aligned}$$

which is precisely the action of T_{24} . Since $S^\dagger = S$ and $S^2 = \mathbf{1}$, we compute

$$\begin{aligned} I_0(SU) &= \text{Tr}(T_{13}) + \text{Tr}[(U^\dagger)^{\otimes 2} S^{\otimes 2} T_{13} S^{\otimes 2} U^{\otimes 2} T_{13}] \\ &= \text{Tr}(T_{13}) + \text{Tr}[(U^\dagger)^{\otimes 2} T_{24} U^{\otimes 2} T_{13}]. \end{aligned} \quad (\text{A9})$$

Comparing with $I_1(U) = \text{Tr}(T_{24}) + \text{Tr}[(U^\dagger)^{\otimes 2} T_{24} U^{\otimes 2} T_{13}]$, we see that $I_0(SU)$ and $I_1(U)$ share the same dynamical term and differ only in their constant parts: $\text{Tr}(T_{13})$ versus $\text{Tr}(T_{24})$. For $d_A = d_B = d$ (as is always the case in the spin chains considered in this work), $\text{Tr}(T_{13}) = \text{Tr}(T_{24}) = d^3$, and therefore

$$I_1(U) = I_0(SU) \quad (d_A = d_B). \quad (\text{A10})$$

To derive the algorithmic form of $\overline{I_1^{(2)}}$, we evaluate $\langle kl|T_{24}|mn\rangle$ directly. The swap operator T_{24} exchanges the two B -factors: $T_{24}|a_1, b_1, a_2, b_2\rangle = |a_1, b_2, a_2, b_1\rangle$. Repeating the index contraction of Sec. A1 with this exchange, we find

$$\begin{aligned} \langle kl|T_{24}|mn\rangle &= \sum_{\substack{a_1, b_1 \\ a_2, b_2}} (C_k)_a^* (C_l)_b (C_i)_{a_2 b_1}^* (C_m)_{a_1 b_1} (C_n)_{a_2 b_2} \\ &= \text{Tr}_B(C_k^\dagger C_m \cdot C_l^\dagger C_n) \\ &= \text{Tr}_B(\hat{M}_i \hat{M}_j^\dagger), \end{aligned} \quad (\text{A11})$$

where $\hat{M}_i \equiv C_{p_i}^\dagger C_{q_i}$ is a $d_B \times d_B$ matrix for the i th pair in the group g_ω . Since T_{13} is Hermitian, $\langle mn|T_{13}|kl\rangle = (\langle kl|T_{13}|mn\rangle)^* = [\text{Tr}_A(M_i^\dagger M_j)]^*$. Combining with Eq. (A11) and summing over the diagonal ensemble as in Sec. A2, each summand takes the form $\text{Tr}_B(\hat{M}_i \hat{M}_j^\dagger) \cdot [\text{Tr}_A(M_i^\dagger M_j)]^*$. Relabeling $i \leftrightarrow j$ in the double sum and using the cyclicity of the trace, this can be rewritten as

$$\overline{I_1^{(2)}} = \sum_\omega \sum_{i,j=1}^{N_\omega} \text{Tr}_A(M_i^\dagger M_j) \cdot \text{Tr}_B(\hat{M}_i^\dagger \hat{M}_j). \quad (\text{A12})$$

Unlike $\overline{I_0^{(2)}}$ in Eq. (A7), the two trace factors in each summand are not complex conjugates of each other, so the expression does not reduce to a modulus squared. The sum is nonetheless real, since the $i \leftrightarrow j$ relabeling complex-conjugates each summand. Equation (A12) is equivalent to the identity (A10) after the same $i \leftrightarrow j$ relabeling.

4. Assembling the time-averaged entangling power

Combining the results above with Eq. (2), the time-averaged entanglement power is

$$\begin{aligned} \overline{\text{ep}} &= 1 - C_{d_A} C_{d_B} \left[\text{Tr}(T_{13}) + \overline{I_0^{(2)}} \right. \\ &\quad \left. + \text{Tr}(T_{24}) + \overline{I_1^{(2)}} \right], \end{aligned} \quad (\text{A13})$$

where $\overline{I_0^{(2)}}$ and $\overline{I_1^{(2)}}$ are given by Eqs. (A7) and (A12), and the constant terms are $\text{Tr}(T_{13}) = d_A d_B^2$ and $\text{Tr}(T_{24}) = d_A^2 d_B$. This completes the derivation of the algorithm.

Appendix B: Spectral decomposition of the spin-1 XYZ Hamiltonian

In this appendix we derive the symmetry decomposition used in Sec. IIID to establish the uniqueness of the XXX degeneracy pattern for spin-1.

1. Discrete symmetry

The general XYZ Hamiltonian (6) does not commute with S_z^{tot} for $a_x \neq a_y$, but it commutes with the parity operators $R_\alpha \equiv e^{i\pi S_{\alpha,1}} \otimes e^{i\pi S_{\alpha,2}}$ for $\alpha = x, y, z$. A π -rotation about the α -axis preserves S_α and flips the other two components,

$$e^{-i\pi S_\alpha} S_\beta e^{i\pi S_\alpha} = \begin{cases} +S_\beta & \beta = \alpha, \\ -S_\beta & \beta \neq \alpha, \end{cases} \quad (\text{B1})$$

so each bilinear term $S_\beta^{(1)} S_\beta^{(2)}$ picks up two sign flips that cancel, giving $[R_\alpha, H] = 0$. The three operators satisfy $R_x R_y R_z = \mathbf{1}$ and $R_\alpha^2 = \mathbf{1}$, generating a $\mathbb{Z}_2 \times \mathbb{Z}_2$ (Klein four-) group.

2. Sector decomposition

For spin-1, R_z has eigenvalue $(-1)^{m_1+m_2}$ on $|m_1, m_2\rangle$, splitting the nine product states into a 5-dimensional even and a 4-dimensional odd sector. The operator R_x acts as $|m_1, m_2\rangle \rightarrow |-m_1, -m_2\rangle$ and commutes with R_z . Forming symmetric and antisymmetric combinations under R_x within each R_z sector yields four blocks. Writing S_x and S_y in terms of $S_{\pm} = S_x \pm iS_y$ and using $H = \frac{a_x+a_y}{4}(S_+^{(1)}S_-^{(2)} + S_-^{(1)}S_+^{(2)}) + \frac{a_x-a_y}{4}(S_+^{(1)}S_+^{(2)} + S_-^{(1)}S_-^{(2)}) + a_z S_z^{(1)}S_z^{(2)}$, we compute the Hamiltonian in each sector.

a. $(R_z, R_x) = (+, +)$, *dimension 3*. In the basis $\{|0, 0\rangle, (|1, 1\rangle + |-1, -1\rangle)/\sqrt{2}, (|1, -1\rangle + |-1, 1\rangle)/\sqrt{2}\}$,

$$H_{(+,+)} = \begin{pmatrix} 0 & \frac{a_x-a_y}{\sqrt{2}} & \frac{a_x+a_y}{\sqrt{2}} \\ \frac{a_x-a_y}{\sqrt{2}} & a_z & 0 \\ \frac{a_x+a_y}{\sqrt{2}} & 0 & -a_z \end{pmatrix}. \quad (\text{B2})$$

This matrix is traceless, so its characteristic polynomial is the depressed cubic polynomial in Eq. (23).

b. $(R_z, R_x) = (+, -)$, *dimension 2*. In the basis $\{(|1, 1\rangle - |-1, -1\rangle)/\sqrt{2}, (|1, -1\rangle - |-1, 1\rangle)/\sqrt{2}\}$,

$$H_{(+,-)} = \begin{pmatrix} a_z & 0 \\ 0 & -a_z \end{pmatrix}, \quad (\text{B3})$$

since the only states that could mediate off-diagonal coupling ($|0, 0\rangle$) belong to the $(+, +)$ sector. The eigenvalues are $\pm a_z$.

c. $(R_z, R_x) = (-, +)$, *dimension 2*. In the basis $\{(|1, 0\rangle + |-1, 0\rangle)/\sqrt{2}, (|0, 1\rangle + |0, -1\rangle)/\sqrt{2}\}$,

$$H_{(-,+)} = \begin{pmatrix} 0 & a_x \\ a_x & 0 \end{pmatrix}, \quad (\text{B4})$$

with eigenvalues $\pm a_x$. (The diagonal vanishes because $S_z^{(1)}S_z^{(2)} = 0$ when one m -value is zero, and the off-diagonal element receives equal contributions $\frac{a_x+a_y}{2}$ and $\frac{a_x-a_y}{2}$ from the flip-flop and $\Delta m = \pm 2$ terms, summing to a_x .)

d. $(R_z, R_x) = (-, -)$, *dimension 2*. In the basis $\{(|1, 0\rangle - |-1, 0\rangle)/\sqrt{2}, (|0, 1\rangle - |0, -1\rangle)/\sqrt{2}\}$,

$$H_{(-,-)} = \begin{pmatrix} 0 & a_y \\ a_y & 0 \end{pmatrix}, \quad (\text{B5})$$

with eigenvalues $\pm a_y$. The off-diagonal element now receives contributions $\frac{a_x+a_y}{2}$ and $-\frac{a_x-a_y}{2}$ (the sign flip from the antisymmetric combination), summing to a_y .

3. Uniqueness of the $\{1, 3, 5\}$ pattern

The full spectrum consists of the three roots of $p(\lambda)$ together with $\pm a_x$, $\pm a_y$, $\pm a_z$. For a 5-fold degenerate

eigenvalue λ_0 to exist, it must appear in all four sectors. From the two-dimensional sectors, $\lambda_0 \in \{\pm a_x\} \cap \{\pm a_y\} \cap \{\pm a_z\}$, which requires $|a_x| = |a_y| = |a_z|$. The identity $p(a_x) = -a_x(a_y - a_z)^2$ shows a_x is a root of p if and only if $a_y = a_z$, with analogous identities for cyclic permutations. Combining these constraints forces $a_x = a_y = a_z$ —the XXX point (up to sign flips from local unitaries).

Appendix C: Analytic entangling power for the spin-1 XXZ model

In this appendix we derive closed-form expressions for both the instantaneous entangling power $\text{ep}(t)$ and its time average $\overline{\text{ep}}$ for the two-site spin-1 XXZ Hamiltonian,

$$H = S_x^{(1)}S_x^{(2)} + S_y^{(1)}S_y^{(2)} + \Delta S_z^{(1)}S_z^{(2)}, \quad (\text{C1})$$

valid for generic values of Δ . The calculation uses the algorithm of Appendix A, together with the $\mathbb{Z}_2 \times \mathbb{Z}_2$ decomposition of Appendix B. We first obtain $\text{ep}(t)$ as an explicit trigonometric polynomial, then recover $\overline{\text{ep}}$ by time averaging.

1. Spectrum and eigenstates

Setting $a_x = a_y = 1$ and $a_z = \Delta$ in the sector Hamiltonians of Appendix B, the $(+, -)$ block (B3) gives eigenvalues $\pm \Delta$, the $(-, +)$ and $(-, -)$ blocks (B4)–(B5) each give ± 1 (since $a_x = a_y = 1$), and the 3×3 $(+, +)$ block (B2) reduces to

$$H_{(+,+)} = \begin{pmatrix} 0 & 0 & \sqrt{2} \\ 0 & \Delta & 0 \\ \sqrt{2} & 0 & -\Delta \end{pmatrix}, \quad (\text{C2})$$

whose characteristic polynomial is $\lambda^3 - (\Delta^2 + 8)\lambda/4 = 0$, giving roots 0 and $E_{\pm} \equiv (-\Delta \pm \zeta)/2$ where $\zeta \equiv \sqrt{\Delta^2 + 8}$. The full spectrum is

$$\{E_n\} = \{\Delta, \Delta, 1, -1, 1, -1, -\Delta, E_+, E_-\}, \quad (\text{C3})$$

listed in the sector order of Appendix B. The corresponding coefficient matrices C_n (3×3 , with rows labeled by the first-site m -value and columns by the second) are

$$C_0 = |1, 1\rangle, \quad C_1 = |-1, -1\rangle, \quad C_6 = \frac{|1, -1\rangle - |-1, 1\rangle}{\sqrt{2}}, \\ C_{2,3} = \frac{|1, 0\rangle \pm |0, 1\rangle}{\sqrt{2}}, \quad C_{4,5} = \frac{|0, -1\rangle \pm |-1, 0\rangle}{\sqrt{2}},$$

for the seven “rational” states ($E = \Delta, \pm 1, -\Delta$), and

$$C_{7,8} = \frac{1}{N_{\pm}} \left(\sqrt{2} |0, 0\rangle + \frac{E_{\pm}}{\sqrt{2}} (|1, -1\rangle + |-1, 1\rangle) \right) \quad (\text{C4})$$

for the E_{\pm} states in the $(+, +)$ sector, with normalization $N_{\pm}^2 = 2 + E_{\pm}^2 = \varsigma(\varsigma \mp \Delta)/2$. The sparsity of these matrices—each has at most two nonzero entries—is the key to making the trace computation tractable.

2. ω -group structure

For generic Δ ($\Delta \notin \{0, \pm 1, \pm 2\}$), all nine eigenvalues are distinct and the $d^4 = 81$ pairs (k, l) partition into 27 ω -groups. Of these, 15 groups involve only the rational states (0–6) and have Δ -independent M -matrices. They decompose as follows: one $\omega = 0$ group (containing 15 pairs, since each of the 9 diagonal pairs has $\omega = 0$ and 6 off-diagonal pairs from the three two-fold degeneracies); two groups at $\omega = \pm 2$ (4 pairs each, from $E_k = 1, E_l = -1$ and vice versa); two at $\omega = \pm 2\Delta$ (2 pairs each); and four at $\omega = \pm(\Delta \pm 1)$ (6 pairs each). The remaining 12 groups each contain 1 or 2 pairs involving at least one E_{\pm} state. These are the “irrational” groups whose traces live in $\mathbb{Q}(\Delta, \varsigma)$.

3. Algebraic structure of the traces

Each trace $\text{Tr}_A(M_i^{\dagger} M_j)$ involves bilinear products of C -matrix entries. For the rational states, these products are in $\mathbb{Q}(\sqrt{2})$ and are Δ -independent. For the E_{\pm} states, the individual entries $\alpha_{\pm} = \sqrt{2}/N_{\pm}$ and $\beta_{\pm}/\sqrt{2} = E_{\pm}/(\sqrt{2}N_{\pm})$ involve irrational normalization factors, but in the traces the square roots cancel and the bilinear products lie in the quadratic extension $\mathbb{Q}(\Delta, \varsigma)$ subject to $\varsigma^2 = \Delta^2 + 8$. For example,

$$\alpha_{\pm}^2 = \frac{4}{\varsigma(\varsigma \mp \Delta)}, \quad \alpha_+ \alpha_- = \frac{\sqrt{2}}{\varsigma}. \quad (\text{C5})$$

The computation then proceeds entirely within $\mathbb{Q}(\Delta, \varsigma)$, with $\varsigma^2 \rightarrow \Delta^2 + 8$ imposed after each intermediate step.

4. The parity factor

The instantaneous entangling power involves the sum $I_0(t) + I_1(t)$, each containing all d^4 quadruples (k, l, k', l') weighted by the phase $e^{-i\Omega t}$ with $\Omega = (E_k - E_l) - (E_{k'} - E_{l'})$. Since every eigenstate has definite site-exchange parity, $C_n^T = \epsilon_n C_n$ with $\epsilon_n = \pm 1$, the \hat{M} -matrix (defined as $\hat{M}_{kl} = C_k^T C_l$) is related to $M_{kl} = C_k C_l^T$ by $\hat{M}_{kl} = \epsilon_k \epsilon_l M_{kl}$. Writing $\sigma_{kl} \equiv \epsilon_k \epsilon_l$:

$$\text{Tr}_A(\hat{M}_{kl}^{\dagger} \hat{M}_{k'l'}) = \sigma_{kl} \sigma_{k'l'} \text{Tr}_A(M_{kl}^{\dagger} M_{k'l'}). \quad (\text{C6})$$

The sum $I_0 + I_1$ then acquires a *parity factor*:

$$I_0(t) + I_1(t) = 2d^3 + \sum_{k, l, k', l'} e^{-i\Omega t} (1 + \sigma_{kl} \sigma_{k'l'}) [\text{Tr}_A(M_{kl}^{\dagger} M_{k'l'})]^2. \quad (\text{C7})$$

This factor takes the value 2 when both pairs share the same exchange parity ($\sigma_{kl} = \sigma_{k'l'}$) and vanishes otherwise: contributions from parity-mismatched pairs cancel between I_0 and I_1 .

The exchange parities of the nine eigenstates are

$$\{\epsilon_n\} = \{+, +, +, -, +, -, -, +, +\}, \quad (\text{C8})$$

where states 0, 1, 2, 4, 7, 8 are symmetric ($C^T = C$) and states 3, 5, 6 are antisymmetric ($C^T = -C$). One can verify that *within* each ω -group, all pairs (k, l) share the same value of σ_{kl} , so the parity factor is uniformly 2 for same-group terms. This is why $\bar{I}_0 = \bar{I}_1$ after time averaging, which restricts to same-group contributions. For cross-group terms ($\Omega \neq 0$), pairs from groups with different σ values are killed by the parity factor.

5. The instantaneous entangling power

Since all coefficient matrices are real, every trace is real and $I_0(t) + I_1(t)$ is a real trigonometric polynomial. The contributions at $+\Omega$ and $-\Omega$ combine into cosines, giving

$$\text{ep}(t) = \frac{5}{8} - \frac{1}{144} \left[\mathcal{A}_0 + \sum_{j=1}^{24} \mathcal{A}_j \cos(\Omega_j t) \right], \quad (\text{C9})$$

with $5/8 = 1 - 2d^3/[d^2(d+1)^2]$ for $d = 3$. The DC component is

$$\mathcal{A}_0 = \frac{46\Delta^4 + 684\Delta^2 + 2636}{(\Delta^2 + 8)^2}, \quad (\text{C10})$$

and the 24 oscillating frequencies fall into 8 rational and 16 irrational terms.

Rational frequencies (8 terms). These arise from beat frequencies among the rational eigenvalues $\{\Delta, 1, -1, -\Delta\}$:

Ω_j	\mathcal{A}_j
Δ	$4/(\Delta^2 + 8)$
$\Delta + 2$	$2\Delta^2/(\Delta^2 + 8)$
$\Delta - 2$	$2\Delta^2/(\Delta^2 + 8)$
$2\Delta + 2$	4
$2\Delta - 2$	4
3Δ	$8/(\Delta^2 + 8)$
4Δ	2
4	3

Irrational frequencies (16 terms). These involve $\varsigma = \sqrt{\Delta^2 + 8}$ and come in conjugate pairs under $\varsigma \rightarrow -\varsigma$: As a consistency check, setting all cosines to 1 (corresponding to $t = 0$, i.e., $U = \mathbf{1}$) gives $\mathcal{A}_0 + \sum_j \mathcal{A}_j = 90$, so that $\text{ep}(0) = 5/8 - 90/144 = 0$, as required.

Ω_j	\mathcal{A}_j
ς	$(52\Delta^2 + 272)/(\Delta^2 + 8)^2$
2ς	$36/(\Delta^2 + 8)^2$
$-\Delta \pm \varsigma$	$(\Delta^2 \pm \Delta\varsigma + 4)/[2(\Delta^2 + 8)]$
$3\Delta \pm \varsigma$	$(\Delta^2 \pm \Delta\varsigma + 4)/(\Delta^2 + 8)$
$(3\Delta \pm \varsigma)/2$	$(6\Delta^2 \pm 2\Delta\varsigma + 48)/(\Delta^2 + 8)$
$\Delta \pm \varsigma + 2$	$8/(\Delta^2 + 8)$
$\Delta \pm \varsigma - 2$	$8/(\Delta^2 + 8)$
$(\Delta \pm \varsigma)/2 + 2$	$(3\Delta^2 \pm \Delta\varsigma + 24)/(\Delta^2 + 8)$
$(\Delta \pm \varsigma)/2 - 2$	$(3\Delta^2 \pm \Delta\varsigma + 24)/(\Delta^2 + 8)$

TABLE III: *Fourier amplitudes and irrational frequencies for the instantaneous entangling power of the spin-1 XXZ model, Eq. (C9). Each “ \pm ” row represents two distinct frequencies (upper and lower signs).*

6. Time averaging and $\overline{\text{ep}}$

Time averaging $\text{ep}(t)$ kills all oscillating terms, leaving only the DC component: $\overline{\text{ep}} = 5/8 - \mathcal{A}_0/144$. Equivalently, this corresponds to restricting the sum in Eq. (C7) to same- ω -group contributions ($\Omega = 0$), for which the parity factor is uniformly 2. This gives $\overline{I_0} + \overline{I_1} = 2\overline{I_0}$, i.e., $\overline{I_0} = \overline{I_1}$ (or equivalently, $I_0^{(2)} = I_1^{(2)}$, see Appendix A 3).

Cancellation of ς . Within each ω -group, the traces involving the E_{\pm} eigenstates live in the quadratic extension $\mathbb{Q}(\Delta, \varsigma)$. However, the 12 irrational groups come in six conjugate pairs related by $\varsigma \rightarrow -\varsigma$ ($E_+ \leftrightarrow E_-$). For example, the pair at $\omega = (3\Delta \mp \varsigma)/2$ contributes

$$\frac{\Delta^2 \mp \Delta\varsigma + 4}{4(\Delta^2 + 8)} \quad (\text{C11})$$

to $\overline{I_0^{(2)}}$. Adding the two conjugates:

$$\frac{\Delta^2 - \Delta\varsigma + 4}{4(\Delta^2 + 8)} + \frac{\Delta^2 + \Delta\varsigma + 4}{4(\Delta^2 + 8)} = \frac{\Delta^2 + 4}{2(\Delta^2 + 8)}, \quad (\text{C12})$$

a rational function of Δ . The same cancellation occurs for every conjugate pair, so all ς -dependence drops out of $\overline{I_0^{(2)}}$.

Result. Summing the 27 ω -group contributions and adding the static part $\text{Tr}(T_{13}) = d^3 = 27$:

$$\overline{I_0^{(2)}} + \text{Tr}(T_{13}) = \frac{23\Delta^4 + 342\Delta^2 + 1318}{(\Delta^2 + 8)^2} + 27, \quad (\text{C13})$$

with $\overline{I_1^{(2)}} + \text{Tr}(T_{24})$ equal to the same value. Inserting into $\overline{\text{ep}} = 1 - [\overline{I_0^{(2)}} + \text{Tr}(T_{13}) + \overline{I_1^{(2)}} + \text{Tr}(T_{24})] / [d^2(d+1)^2]$ with $d = 3$ gives Eq. (18) in the main text. This expression is manifestly positive, symmetric under $\Delta \rightarrow -\Delta$, and monotonically increasing toward 11/36 as $|\Delta| \rightarrow \infty$. It has been verified numerically at $\Delta = 1/2$ (yielding

4421/13068) and $\Delta = 3$ (yielding 3373/10404), as well as at $\Delta = 3/2$ and numerous other non-degenerate values.

It is worth pointing out that the time average of $\text{ep}(t)$ provides an independent derivation of $\overline{\text{ep}}$: one simply reads off the constant term from Eq. (C9), bypassing the need to sum ω -group contributions and cancel ς explicitly.

7. Validity and degenerate points

Both Eq. (C9) and Eq. (18) were derived under the assumption that the 27 ω -groups are all distinct. At special values of Δ where eigenvalue differences coincide—namely $\Delta = 0, \pm 1$, and ± 2 —some groups merge and the cross-terms between formerly separate groups contribute additional positive terms to $I_0^{(2)}$. Since $\overline{\text{ep}}$ decreases with increasing $I_0 + I_1$, the true value at these degenerate points lies *below* the generic formula. The magnitude of the drop depends on the extent of the degeneracy: at $\Delta = \pm 1$, where the number of groups drops from 27 to 7, the XXX point has $\overline{\text{ep}} = 13/54 \approx 0.241$ versus the generic-formula value of $981/2916 \approx 0.336$; at $\Delta = \pm 2$, where 27 groups reduce to 25, the drop is much milder ($\overline{\text{ep}} \approx 0.326$ versus 0.330).

Equation (18) thus provides the “background curve” of $\overline{\text{ep}}$ as a smooth function of the anisotropy. The sharp dips at $\Delta = 0$ and ± 1 discussed in the main text are superimposed on this background as measure-zero discontinuities of the infinite-time average, arising from accidental eigenvalue degeneracies that enlarge the ω -groups.

Appendix D: Bethe Ansatz and the Two-Magnon S -matrix

This appendix provides a self-contained derivation of the two-magnon scattering matrix for the spin-1/2 XXZ chain starting from the coordinate Bethe ansatz [61]. The presentation follows the standard treatment in Refs. [75–77]; we include it here because the Bethe ansatz framework may be less familiar to readers approaching spin chains from the quantum-information perspective. Following the Bethe ansatz literature, we write S_j^α for the spin operator at site j (rather than $S_{\alpha,j}$ used in the main text).

1. Setup and the ferromagnetic vacuum

We consider the spin-1/2 XXZ Hamiltonian on a periodic chain of L sites:

$$H_{\text{XXZ}} = \sum_{j=1}^L (S_j^x S_{j+1}^x + S_j^y S_{j+1}^y + \Delta S_j^z S_{j+1}^z), \quad (\text{D1})$$

with periodic boundary conditions $\vec{S}_{L+1} \equiv \vec{S}_1$ and anisotropy parameter $\Delta = \cos \gamma$ with

$\gamma \in [0, \pi]$.

The Hamiltonian conserves the total spin projection $S_{\text{tot}}^z = \sum_j S_j^z$, which allows diagonalization within sectors of fixed M down-spins. The fully polarized state $|\Omega\rangle \equiv |\uparrow\uparrow \cdots \uparrow\rangle$ is an eigenstate with energy $E_0 = \frac{1}{4}L\Delta$, and serves as the reference vacuum. Spin-flip excitations above this vacuum are called magnons.

2. One-magnon sector

A single spin flip at site n creates the state $|n\rangle \equiv S_n^- |\Omega\rangle$. Acting with the Hamiltonian on the ansatz $|\psi\rangle = \sum_{n=1}^L \phi(n) |n\rangle$ yields the eigenvalue equation

$$\frac{1}{2}[\phi(n+1) + \phi(n-1)] + \frac{1}{4}(L-2)\Delta\phi(n) - \frac{1}{2}\Delta\phi(n) = E\phi(n). \quad (\text{D2})$$

Substituting the plane-wave ansatz $\phi(n) = e^{ipn}$ immediately gives the magnon dispersion relation

$$\epsilon(p) \equiv E - E_0 = \Delta - \cos p, \quad (\text{D3})$$

where $\epsilon(p)$ is the magnon energy measured relative to the vacuum. The quasi-momentum p is quantized by the periodic boundary condition: $e^{ipL} = 1$, so $p = 2\pi m/L$ with $m = 0, 1, \dots, L-1$.

3. Two-magnon sector and the Bethe wavefunction

Two magnons at positions $n_1 < n_2$ define the state $|n_1, n_2\rangle = S_{n_1}^- S_{n_2}^- |\Omega\rangle$. In the region $n_2 - n_1 \geq 2$, where the two flipped spins do not occupy adjacent sites, each magnon propagates independently and the eigenvalue equation reduces to two copies of the one-magnon problem. The Bethe ansatz wavefunction in this region is a superposition of incoming and outgoing plane waves:

$$\psi(n_1, n_2) = A e^{i(p_1 n_1 + p_2 n_2)} + B e^{i(p_2 n_1 + p_1 n_2)}, \quad (\text{D4})$$

where p_1 and p_2 are the quasi-momenta of the two magnons, A is the amplitude for the “direct” configuration (magnon 1 to the left with momentum p_1), and B is the amplitude for the “exchanged” configuration (momenta swapped). The total energy is the sum of individual magnon energies:

$$E - E_0 = \epsilon(p_1) + \epsilon(p_2) = 2\Delta - \cos p_1 - \cos p_2. \quad (\text{D5})$$

The nontrivial physics arises when the two magnons are adjacent, $n_2 = n_1 + 1$. In this case the exchange terms in the Hamiltonian produce a contact interaction: the eigenvalue equation at the boundary $n_2 = n_1 + 1$ differs from the bulk equation by an additional term proportional to Δ . Substituting the ansatz (D4) into the boundary condition and requiring consistency with the bulk equation yields the scattering amplitude ratio

$$\frac{B}{A} = -\frac{e^{i(p_1+p_2)} - 2\Delta e^{ip_2} + 1}{e^{i(p_1+p_2)} - 2\Delta e^{ip_1} + 1} \equiv -e^{i\phi(p_1, p_2)}, \quad (\text{D6})$$

where $\phi(p_1, p_2)$ is the two-magnon scattering phase. The key observation of Bethe [61] is that this ratio is a *pure phase*: $|B/A| = 1$. Physically, this means magnons scattering in the XXZ chain is purely elastic—magnons exchange momenta but are never reflected or absorbed. This is the hallmark of integrability.

The quantization conditions on a periodic chain of length L are the *Bethe equations*:

$$e^{ip_1 L} = -\frac{B}{A}, \quad e^{ip_2 L} = -\frac{A}{B}, \quad (\text{D7})$$

which state that the phase accumulated by each magnon around the chain equals the product of all pairwise scattering phases.

4. Spectral parameter, rapidity, and the R -matrix

The scattering phase (D6) can be greatly simplified by trading the quasi-momenta p_j for the trigonometric *spectral parameter* u_j , defined by [75, 77]

$$e^{ip_j} = \frac{\sin(u_j + \gamma/2)}{\sin(u_j - \gamma/2)}. \quad (\text{D8})$$

Substituting into the scattering amplitude (D6) yields, after straightforward algebra,

$$\frac{B}{A} = \frac{\sin(u_{12} - \gamma)}{\sin(u_{12} + \gamma)}, \quad (\text{D9})$$

where $u_{12} \equiv u_1 - u_2$. This depends only on the *difference* of the spectral parameters, which is the hallmark of integrability: the scattering is a function of the relative rapidity alone.

In the isotropic limit $\gamma \rightarrow 0$ ($\Delta \rightarrow 1$), the spectral parameter reduces to the rational Bethe rapidity. Writing $u_j = \gamma\lambda_j$ and taking $\gamma \rightarrow 0$ in Eq. (D8) gives $e^{ip_j} \rightarrow (\lambda_j + \frac{1}{2}i)/(\lambda_j - \frac{1}{2}i)$, which inverts to $\lambda_j = \frac{1}{2} \cot(p_j/2)$. In this limit Eq. (D9) becomes $B/A \rightarrow (\lambda_{12} - i)/(\lambda_{12} + i)$, recovering the familiar rational form of the XXX scattering phase.

To construct the full two-body scattering matrix, we note that the XXZ Hamiltonian conserves S_{tot}^z . In the two-magnon sector, the Hilbert space at each pair of sites decomposes into sectors of total $S^z = +1, 0, -1$. The $S^z = \pm 1$ sectors (both spins aligned) are one-dimensional and trivially scatter with unit amplitude. The $S^z = 0$ sector is two-dimensional, spanned by $|\uparrow\downarrow\rangle$ and $|\downarrow\uparrow\rangle$, and it is here that the nontrivial scattering takes place.

Writing the S -matrix on $\mathbb{C}^2 \otimes \mathbb{C}^2$ in the computational basis $\{|\uparrow\uparrow\rangle, |\uparrow\downarrow\rangle, |\downarrow\uparrow\rangle, |\downarrow\downarrow\rangle\}$ yields the six-vertex R -matrix:

$$R(u, \gamma) = \begin{pmatrix} a & 0 & 0 & 0 \\ 0 & b & c & 0 \\ 0 & c & b & 0 \\ 0 & 0 & 0 & a \end{pmatrix}, \quad (\text{D10})$$

with vertex weights $a = \sin(u + \gamma)$, $b = \sin u$, $c = \sin \gamma$, where u is the spectral-parameter difference u_{12} defined above. The name ‘‘six-vertex’’ refers to the six nonzero matrix elements, which correspond to the six allowed arrow configurations in the ice-type vertex model [64, 65, 78]. The anisotropy is encoded by $\Delta = \cos \gamma$.

5. Yang–Baxter equation

The integrability of the XXZ chain is ultimately guaranteed by the Yang–Baxter equation [65, 67, 68]:

$$R_{12}(u_{12}) R_{13}(u_{13}) R_{23}(u_{23}) = R_{23}(u_{23}) R_{13}(u_{13}) R_{12}(u_{12}), \quad (\text{D11})$$

where $u_{ij} \equiv u_i - u_j$ and R_{jk} acts on spaces j and k . Equation (D11) is a matrix equation in $(\mathbb{C}^2)^{\otimes 3}$ and states that the order of pairwise scatterings in a three-body collision does not affect the outcome.

The physical consequence is factorized scattering [66, 77]: the N -magnon S -matrix decomposes into a product of $\binom{N}{2}$ two-body S -matrices, and the Bethe equations (D7) generalize to N coupled equations whose consistency is precisely the Yang–Baxter equation. This is the algebraic foundation of integrability in the XXZ chain.

We note in passing that the quantum group symmetry $U_q(\mathfrak{sl}_2)$ discussed in Sec. IV C is intimately connected to the R -matrix: the Yang–Baxter equation is the defining relation of the quasi-triangular Hopf algebra structure of $U_q(\mathfrak{sl}_2)$, and the six-vertex R -matrix is its fundamental representation [41–43].

6. From R -matrix to physical S -matrix

The R -matrix (D10) is not unitary for real spectral parameter u , as the vertex weights are in general complex. To obtain the physical unitary S -matrix appropriate for real-time scattering, we analytically continue $u \rightarrow i\theta$, where θ is the rapidity difference of the two magnons. This yields the vertex weights

$$\begin{aligned} a &= \sin(i\theta + \gamma) = i \sinh \theta \cos \gamma + \cosh \theta \sin \gamma, \\ b &= \sin(i\theta) = i \sinh \theta, \\ c &= \sin \gamma. \end{aligned} \quad (\text{D12})$$

Normalizing by $\rho \equiv \sqrt{\sin^2 \gamma + \sinh^2 \theta}$ yields the unitary S -matrix $S(\theta, \gamma) = R(i\theta, \gamma)/\rho$, which is the matrix studied in Sec. VI. The three eigenvalue phases φ_+ , φ_t , and φ_s discussed in Sec. VI B are the arguments of the eigenvalues of this unitary matrix.

7. Entangling power of the S -matrix

We derive the entangling power formula Eq. (41) for any $U(1)$ -conserving two-qubit unitary with eigenvalue

phase differences δ_{t+} and δ_{s+} . For $d_A = d_B = 2$ the identity $1 - \text{Tr}(\rho_A^2) = 2 \det \rho_A$ simplifies the entangling power to

$$\text{ep}(U) = 4 \int d\mu(\psi) d\mu(\phi) \det \rho_A, \quad (\text{D13})$$

where $d\mu(\psi)$ and $d\mu(\phi)$ denote independent Haar measures on \mathbb{C}^2 .

Since the overall phase φ_+ drops out of the entangling power, the S -matrix in the computational basis takes the effective form $\text{diag}(1, B, B, 1)$ with off-diagonal entries in the $S^z = 0$ block given by the spin-exchange amplitude C , where $B = (e^{i\delta_{t+}} + e^{i\delta_{s+}})/2$, $C = (e^{i\delta_{t+}} - e^{i\delta_{s+}})/2$, and $|B|^2 + |C|^2 = 1$, $\text{Re}(B^*C) = 0$. Parametrize the Haar-random input states on the Bloch sphere as $|\psi\rangle = \cos \frac{\alpha}{2} |0\rangle + e^{i\xi} \sin \frac{\alpha}{2} |1\rangle$ and $|\phi\rangle = \cos \frac{\beta}{2} |0\rangle + \sin \frac{\beta}{2} |1\rangle$, with polar angles $\alpha, \beta \in [0, \pi]$ and azimuthal angle $\xi \in [0, 2\pi)$, where the $U(1)$ symmetry has been exploited to fix the azimuthal angle of $|\phi\rangle$. Writing $p = \cos^2 \frac{\alpha}{2}$ and $q = \cos^2 \frac{\beta}{2}$ for compactness, the output state vector $U|\psi\rangle|\phi\rangle$ has components whose reduced density matrix ρ_A satisfies

$$\det \rho_A = |e^{i\xi} w F + G [p(1-q) + e^{2i\xi}(1-p)q]|^2, \quad (\text{D14})$$

where $w = \sqrt{p(1-p)q(1-q)} = \frac{1}{4} \sin \alpha \sin \beta$ and

$$F = 1 - e^{i(\delta_{t+} + \delta_{s+})} \cos(\delta_{t+} - \delta_{s+}), \quad (\text{D15})$$

$$G = -\frac{i}{2} e^{i(\delta_{t+} + \delta_{s+})} \sin(\delta_{t+} - \delta_{s+}). \quad (\text{D16})$$

The Haar measure on each Bloch sphere is $d\mu = \frac{1}{4\pi} \sin \alpha d\alpha d\xi$, so the integral (D13) becomes $\text{ep} = 4 \int_0^\pi \frac{\sin \alpha d\alpha}{2} \int_0^\pi \frac{\sin \beta d\beta}{2} \int_0^{2\pi} \frac{d\xi}{2\pi} |\det \rho_A|$, i.e. a uniform average over p , q , and ξ . A key simplification is that all cross-terms between the F and G contributions contain factors of $e^{\pm i\xi}$ or $e^{\pm 3i\xi}$, which vanish upon ξ -integration. This leaves

$$\text{ep} = 4 \left[\frac{|F|^2}{36} + \frac{2|G|^2}{9} \right], \quad (\text{D17})$$

where we have used the Bloch-sphere moments $\langle p(1-p) \rangle = 1/6$ and $\langle p^2 \rangle = 1/3$, with $\langle \cdot \rangle$ denoting the average over the uniform measure on $[0, 1]$.

Substituting $|F|^2 = 1 - 2 \cos(\delta_{t+} + \delta_{s+}) \cos(\delta_{t+} - \delta_{s+}) + \cos^2(\delta_{t+} - \delta_{s+})$ and $|G|^2 = \sin^2(\delta_{t+} - \delta_{s+})/4$, we obtain

$$\begin{aligned} \text{ep}(\delta_{t+}, \delta_{s+}) &= \frac{1}{9} \left[1 - 2 \cos(\delta_{t+} + \delta_{s+}) \cos(\delta_{t+} - \delta_{s+}) \right. \\ &\quad \left. + \cos^2(\delta_{t+} - \delta_{s+}) + 2 \sin^2(\delta_{t+} - \delta_{s+}) \right] \\ &= \frac{1}{9} \left[3 - 2 \cos(\delta_{t+} + \delta_{s+}) \cos(\delta_{t+} - \delta_{s+}) \right. \\ &\quad \left. - \cos^2(\delta_{t+} - \delta_{s+}) \right], \end{aligned} \quad (\text{D18})$$

which is Eq. (41).

- [1] S. R. Beane, D. B. Kaplan, N. Klco, and M. J. Savage, Phys. Rev. Lett. **122**, 102001 (2019), arXiv:1812.03138 [hep-ph] .
- [2] I. Low and T. Mehen, Phys. Rev. D **104**, 074014 (2021), arXiv:2104.10835 [hep-ph] .
- [3] Q. Liu, I. Low, and T. Mehen, Phys. Rev. C **107**, 025204 (2023), arXiv:2210.12085 [hep-ph] .
- [4] Q. Liu, I. Low, and Z. Yin, Phys. Rev. D **111**, 065027 (2025), arXiv:2410.22414 [hep-ph] .
- [5] T.-R. Hu, K. Sone, F.-K. Guo, T. Hyodo, and I. Low, (2025), arXiv:2506.08960 [hep-ph] .
- [6] M. Carena, I. Low, C. E. M. Wagner, and M.-L. Xiao, Phys. Rev. D **109**, L051901 (2024), arXiv:2307.08112 [hep-ph] .
- [7] M. Carena, G. Coloretti, W. Liu, M. Lippmann, I. Low, and C. E. M. Wagner, JHEP **08**, 016, arXiv:2505.00873 [hep-ph] .
- [8] G. Busoni, J. Gargalionis, E. N. V. Wallace, and M. J. White, Phys. Rev. D **112**, 035022 (2025), arXiv:2506.01314 [hep-ph] .
- [9] C. Li, T. Ma, J. Shu, and M. Zhu, (2026), arXiv:2605.17434 [hep-ph] .
- [10] N. McGinnis, (2025), arXiv:2504.21079 [hep-th] .
- [11] N. McGinnis, (2025), arXiv:2511.10559 [hep-th] .
- [12] J. Thaler and S. Trifinopoulos, Phys. Rev. D **111**, 056021 (2025), arXiv:2410.23343 [hep-ph] .
- [13] Q. Liu, I. Low, and Z. Yin, (2025), arXiv:2509.18251 [hep-ph] .
- [14] J. Liu, M. Tanaka, X.-P. Wang, J.-J. Zhang, and Z. Zheng, (2025), arXiv:2511.17321 [hep-ph] .
- [15] P. Calabrese and J. L. Cardy, J. Stat. Mech. **0406**, P06002 (2004), arXiv:hep-th/0405152 .
- [16] P. Calabrese and J. Cardy, J. Phys. A **42**, 504005 (2009), arXiv:0905.4013 [cond-mat.stat-mech] .
- [17] G. Vidal, J. I. Latorre, E. Rico, and A. Kitaev, Phys. Rev. Lett. **90**, 227902 (2003), arXiv:quant-ph/0211074 .
- [18] J. I. Latorre, E. Rico, and G. Vidal, Quant. Inf. Comput. **4**, 48 (2004), arXiv:quant-ph/0304098 .
- [19] A. Osterloh, L. Amico, G. Falci, and R. Fazio, Nature **416**, 608 (2002).
- [20] T. J. Osborne and M. A. Nielsen, Phys. Rev. A **66**, 032110 (2002).
- [21] L. Amico, R. Fazio, A. Osterloh, and V. Vedral, Rev. Mod. Phys. **80**, 517 (2008), arXiv:quant-ph/0703044 .
- [22] J. Eisert, M. Cramer, and M. B. Plenio, Rev. Mod. Phys. **82**, 277 (2010), arXiv:0808.3773 [quant-ph] .
- [23] M. Goldstein and E. Sela, Phys. Rev. Lett. **120**, 200602 (2018), arXiv:1711.09418 [cond-mat.stat-mech] .
- [24] J. C. Xavier and F. C. Alcaraz, Phys. Rev. B **98**, 041106 (2018), arXiv:1804.06357 [cond-mat.stat-mech] .
- [25] S. Murciano, G. Di Giulio, and P. Calabrese, SciPost Phys. **8**, 046 (2020), arXiv:1911.09588 [cond-mat.stat-mech] .
- [26] F. Ares, S. Murciano, and P. Calabrese, Nature Commun. **14**, 2036 (2023), arXiv:2207.14693 [cond-mat.stat-mech] .
- [27] P. Zanardi, C. Zalka, and L. Faoro, Phys. Rev. A **62**, 030301 (2000).
- [28] P. Zanardi, Phys. Rev. A **63**, 040304 (2001), arXiv:quant-ph/0010074 .
- [29] R. Pal and A. Lakshminarayan, Phys. Rev. B **98**, 174304 (2018), arXiv:1805.11632 [quant-ph] .
- [30] S. Pal and A. Lakshminarayan, Phys. Rev. A **110**, 042602 (2024), arXiv:2407.07897 [quant-ph] .
- [31] M. A. Nielsen and I. L. Chuang, *Quantum Computation and Quantum Information* (Cambridge University Press, 2012).
- [32] G. Styliaris, N. Anand, and P. Zanardi, Phys. Rev. Lett. **126**, 030601 (2021), arXiv:2007.08570 [quant-ph] .
- [33] H.-X. Lu, L.-N. Wang, and X. Wang, Phys. Rev. A **78**, 032309 (2008).
- [34] S. Hill and W. K. Wootters, Phys. Rev. Lett. **78**, 5022 (1997), arXiv:quant-ph/9703041 .
- [35] W. K. Wootters, Phys. Rev. Lett. **80**, 2245 (1998), arXiv:quant-ph/9709029 .
- [36] R. Orbach, Phys. Rev. **112**, 309 (1958).
- [37] P. Jordan and E. Wigner, Z. Phys. **47**, 631 (1928).
- [38] E. Lieb, T. Schultz, and D. Mattis, Ann. Phys. **16**, 407 (1961).
- [39] E. Lieb, T. Schultz, and D. Mattis, Annals Phys. **16**, 407 (1961).
- [40] S. D. Pace, A. Chatterjee, and S.-H. Shao, (2024), arXiv:2412.18606 [cond-mat.str-el] .
- [41] V. G. Drinfel'd, Sov. Math. Dokl. **32**, 254 (1985).
- [42] M. Jimbo, Lett. Math. Phys. **10**, 63 (1985).
- [43] V. Chari and A. Pressley, *A Guide to Quantum Groups* (Cambridge University Press, 1994).
- [44] J. Lamers, PoS **Modave2014**, 001 (2014), arXiv:1501.06805 [math-ph] .
- [45] V. Pasquier and H. Saleur, Nucl. Phys. B **330**, 523 (1990).
- [46] F. C. Alcaraz, M. N. Barber, and M. T. Batchelor, Ann. Phys. **182**, 280 (1988).
- [47] T. Deguchi, K. Fabricius, and B. M. McCoy, J. Stat. Phys. **102**, 701 (2001), arXiv:cond-mat/9912141 .
- [48] F. D. M. Haldane, Phys. Rev. Lett. **50**, 1153 (1983).
- [49] I. Affleck, T. Kennedy, E. H. Lieb, and H. Tasaki, Phys. Rev. Lett. **59**, 799 (1987).
- [50] I. Affleck, T. Kennedy, E. H. Lieb, and H. Tasaki, Commun. Math. Phys. **115**, 477 (1988).
- [51] G. V. Uimin, JETP Lett. **12**, 225 (1970).
- [52] C. K. Lai, J. Math. Phys. **15**, 1675 (1974).
- [53] B. Sutherland, Phys. Rev. B **12**, 3795 (1975).
- [54] L. A. Takhtajan, Phys. Lett. A **87**, 479 (1982).
- [55] H. M. Babujian, Phys. Lett. A **90**, 479 (1982).
- [56] H. N. V. Temperley and E. H. Lieb, Proc. Roy. Soc. Lond. A **322**, 251 (1971).
- [57] M. N. Barber and M. T. Batchelor, Phys. Rev. B **40**, 4621 (1989).
- [58] A. Klümper, J. Phys. A **23**, 809 (1990).
- [59] P. Martin, *Potts Models and Related Problems in Statistical Mechanics* (World Scientific, 1991).
- [60] V. Alba and P. Calabrese, Proc. Natl. Acad. Sci. U.S.A. **114**, 7947 (2017), arXiv:1608.00614 [cond-mat.stat-mech] .
- [61] H. Bethe, Z. Phys. **71**, 205 (1931).
- [62] C. N. Yang and C. P. Yang, Phys. Rev. **150**, 321 (1966).
- [63] J. des Cloizeaux and J. J. Pearson, Phys. Rev. **128**, 2131 (1962).
- [64] E. H. Lieb, Phys. Rev. Lett. **18**, 692 (1967).
- [65] R. J. Baxter, Ann. Phys. **70**, 193 (1972).
- [66] A. B. Zamolodchikov and A. B. Zamolodchikov, Ann.

- Phys. **120**, 253 (1979).
- [67] C. N. Yang, Phys. Rev. Lett. **19**, 1312 (1967).
- [68] E. K. Sklyanin, L. A. Takhtajan, and L. D. Faddeev, Theor. Math. Phys. **40**, 688 (1979).
- [69] J. Zhang, J. Vala, S. Sastry, and K. B. Whaley, Phys. Rev. A **67**, 042313 (2003), arXiv:quant-ph/0209120 .
- [70] S. Balakrishnan and R. Sankaranarayanan, Phys. Rev. A **82**, 034301 (2010), arXiv:1005.2467 [quant-ph] .
- [71] I. Bloch, J. Dalibard, and S. Nascimbène, Nature Phys. **8**, 267 (2012).
- [72] C. Gross and I. Bloch, Science **357**, 995 (2017).
- [73] C. Monroe, W. C. Campbell, L.-M. Duan, Z.-X. Gong, A. V. Gorshkov, P. W. Hess, R. Islam, K. Kim, N. M. Linke, G. Pagano, P. Richerme, C. Senko, and N. Y. Yao, Rev. Mod. Phys. **93**, 025001 (2021), arXiv:1912.07845 [quant-ph] .
- [74] C. Bai, Z. Zhou, B. Lapierre, and S. Ryu, (2026), arXiv:2604.01296 [quant-ph] .
- [75] V. E. Korepin, N. M. Bogoliubov, and A. G. Izergin, *Quantum Inverse Scattering Method and Correlation Functions* (Cambridge University Press, 1993).
- [76] M. Gaudin, *The Bethe Wavefunction* (Cambridge University Press, 2014).
- [77] L. D. Faddeev, Les Houches Lectures 1995 , 149 (1996), arXiv:hep-th/9605187 .
- [78] E. H. Lieb, Phys. Rev. **162**, 162 (1967).